Analysis of Uranium Oxide Weathering by Molecular Spectroscopy

Thesis

Matthew S. Zickafoose, Captain, USAF

AFIT/GAP/ENP/97D-10

DEPARTMENT OF THE AIR FORCE
AIR UNIVERSITY
AIR FORCE INSTITUTE OF TECHNOLOGY

Wright-Patterson Air Force Base, Ohio

Analysis of Uranium Oxide Weathering by Molecular Spectroscopy

Thesis

Matthew S. Zickafoose, Captain, USAF

AFIT/GAP/ENP/97D-10

Analysis of Uranium Oxide Weathering by Molecular Spectroscopy

Thesis

Presented to the Faculty of the Graduate School of Engineering

of the Air Force Institute of Technology

Air University

Air Education and Training Command

In Partial Fulfillment of the Requirements for the

Degree of Master of Science in Nuclear Physics

Matthew S. Zickafoose, B.S.

Captain, USAF

November 1997

Analysis of Uranium Oxide Weathering by Molecular Spectroscopy

Matthew S. Zickafoose, B.S.
Captain, USAF

Approved:

Chairman	24 Nov 97 Date
	24 Nov 97 Date
	24 Nov 97 Date

Acknowledgments

I would like to express my sincerest appreciation and gratitude to my faculty advisor Major Jeffrey Martin and the members of my committee, Dr. Larry Burggraf and Commander Mike Susalla, for their guidance and support throughout the course of this thesis effort. I would like to thank the sponsors of this thesis effort, the Air Force Technical Applications Center, for the support and latitude provided me in this effort.

I wish to convey a special thanks to Dr. DeLyle Eastwood for her undying effort to support this thesis effort. Without her assistance, much of the progress made in this thesis would not have occurred. Her experience in the techniques of molecular spectroscopy and chemistry were invaluable. Also, I wish to thank Mr. Leroy Cannon for his assistance in the laboratory.

Most importantly, I need to express my thanks to my wife, Lorelei, and daughter, Alexis, whose love and understanding has allowed me to focus on my studies over the last eighteen months. Without their support, and prodding, this experience would not have been as fruitful.

Matthew S. Zickafoose

Table of Contents

List of Figures

List of Tables

Abstract

A preliminary study of the weathering of uranium oxide particles diluted in diamond dust at ambient environmental conditions is presented. The primary weathering reaction is oxidation of the uranium from the +4 to +6 oxidation state, although formation of compounds such as carbonates and hydroxides is possible. Identification of the state of uranium oxides has been attempted using luminescence spectroscopy and diffuse reflectance infrared Fourier transform spectroscopy (DRIFTS). Luminescence spectra of nominal samples of three common oxides, UO_3, U_3O_8, and UO_2, have been measured showing significant spectral differences in peaks at 494 nm, 507 nm, 529 nm, and 553 nm. DRIFTS spectra of the same three oxides show significant differences in peaks at 960 cm^{-1}, 856 cm^{-1}, and 756 cm^{-1}. The differences in these peaks will allow determination of the oxidation to the +6 state in these compounds.

Analysis of Uranium Oxide Weathering by Molecular Spectroscopy

I. Introduction

A. Problem

One of the most important fuels for nuclear fission reactors is uranium dioxide. This ceramic is the product of the front end of the nuclear fuel cycle. The ceramic is packaged as a small pellet and placed into long cladding tubes which are the individual fuel pins for the reactors. It is possible, that at this point in the fuel cycle, a small portion of the uranium dioxide escapes the fuel cycle and enters the environment. What happens to that uranium dioxide once it escapes the nuclear fuel cycle? What effects do the environment have on the uranium dioxide? Is there a way to tell how long a particle has been exposed to the environment? If there is a way to determine how long a particle has been exposed to the environment, then the ability to date these particles is also available. The age of the particle is important since determination of that age can aid in the monitoring of nuclear weapons proliferation.

One possible method of dating UO_2 particles is to determine the amount of oxidation that these particles undergo after they have left the fuel cycle. It is known that UO_2 oxidizes to UO_3 when exposed to oxygen [COL/84]. This oxidation is a gradual process which begins at the outside of the particle and proceeds through the depth of the particle. If the rate of oxidation can be determined, a method for dating a particle after exposure to the environment can be established.

In order to study the weathering of uranium oxide particles, those particles have to be oxidized in a controlled manner. For this oxidation, a method for weathering the particles is developed. To determine if oxidation has occurred, molecular spectroscopy techniques are utilized. The techniques chosen for this analysis are diffuse reflectance Fourier transform spectroscopy (DRIFTS), photoluminescence spectroscopy and Raman scattering.

B. Scope

This analysis is concerned with the oxidation rate of UO_2 particles, with a size range of 1 to 20 microns, in controlled environmental conditions. Variation in environmental conditions consists of three different gas compositions, two relative humidifies, three temperatures and two levels of ultra-violet exposure. The applications of diffuse reflectance infrared Fourier transform spectroscopy (DRIFTS), photoluminescence spectroscopy, and Raman scattering are three complimentary molecular spectroscopy techniques used to determine the level of oxidation in this study. In order to accomplish the weathering of the UO_2 particles, a weathering apparatus and technique specific exposure cells were designed to allow exposure to controlled environmental conditions, and also provide containment of the radioactive substance.

Also, this study is concerned with the exposure of cerium dioxide (CeO_2) particles to the same environmental conditions to provide a non-hazardous actinide simulant for surface deposition concerns. The CeO_2 is not expected to undergo any oxidation, as it is already in the most stable oxidation state, however, it provides a substrate for the deposition of compounds that are by-products of the environmental conditions.

C. Background

Environmental conditions are thought to have important effects on the rate of oxidation of UO_2. The conditions which affect the oxidation rate include oxygen concentration, carbon dioxide concentration, humidity, temperature [RIT/81] and ultra-violet exposure. Since the concentration of these components vary widely with climate throughout the world, it will be important to the dating process to determine the impact of each parameter on the oxidation rate.

There are three types of hazards to be concerned with in this analysis. They are radiological concerns, toxicity concerns, and particulate size concerns. Radiological concerns are obvious since we are dealing with natural uranium. However, with the amounts of material used in this analysis, the exposure risks are minimal. Natural uranium is predominantly an alpha emitter, from U-238. Shielding of the radiation can be accomplished by placing a piece of paper between the source and any worker involved.

Heavy metal toxicity is of more concern than are the radiological concerns. The guidelines for uranium toxicity state "human contact not to exceed 0.2 mg/m^3 as soluble or insoluble compounds containing natural uranium" [WEA/85]. To avoid contact with the material, gloves are worn at all times when handling the material or its containers. The third concern is due to the size of the particles. With a size range of 1 to 20 microns, there is a hazard of inhalation. If the uranium compound is inhaled into the lungs, the precautions against the radiological and toxicity concerns are insufficient. To prevent inhalation from occurring, a respirator is worn at all times the material is transported, or outside of a containment chamber. Also goggles and gloves are worn to limit possible exposure to the eyes and hands.

The chemical state of uranium in a particle can be determined using a number of chemical instrumentation techniques. Uranium has four oxidation, or valence states. These are +3, +4, +5, and +6. The value of the oxidation state identifies the number of electrons that the atom has available to bond with other atoms. A UO_2 compound would have the uranium in the +4 oxidation state. Further, to be in the +3 oxidation state, the compound, with oxygen, would be U_2O_3, the +5 oxidation state yields U_2O_5, and the +6 oxidation state yields UO_3. The compounds of U_2O_3 and U_2O_5 are not common. The trivalent uranium ion reduces water to hydrogen, therefore, stable aqueous solutions of trivalent uranium compounds cannot be formed. The pentavalent uranium compounds disproportionate readily into the tetrravalent and hexavalent forms. It is also known that non-stoichiometric compounds of uranium and oxygen exist [COL/84]. In fact, the non-stoichiometric are the more common compounds. The most common non-stoichiometric compound is U_3O_8, which is equivalent to $UO_{2.66}$. It is a combination of the +4 and +6 oxidation states of uranium. This form occurs naturally in the mineral pitchblende. U_3O_8 is the most common oxide of uranium found in nature because it has the highest heat capacity, the highest value of entropy, and the lowest Gibb's free energy of the uranium oxides [WEA/85].

The non-stoichiometric molecules are what we are most interested in. It has been stated by Colmenares [COL/84] that UO_2, when exposed to a pure oxygen environment proceeds to $UO_{2.06}$ almost instantaneously, and when exposed to a oxygen/H_2O(v) environment, proceeds to UO_{2+x} ($0.12 \leq x \leq 0.20$)

upon contact with oxygen. From there, it proceeds, non-stoichiometrically, until it reaches UO_3. UO_3 is the most stable form of uranium oxide.

The use of cerium dioxide is intended to limit the radiation exposure for this thesis. The intent is to use cerium dioxide as an actinide simulant to proof test the procedures developed for use with the uranium. Cerium dioxide films are important component of solar energy cells. There have been several studies that deal with these CeO_2 films, but very few that deal with CeO_2 particles.

The size of the particles of the uranium oxides for this study is between 1 and 20 microns. The particle sizes of the CeO_2 range in size from 3 to 10 microns. Scanning electron microscope images of the CeO_2 particles are shown in Appendix B. Scanning electron microscope images of the uranium oxides are not available due to the radiation requirements in effect at this location. Concern about particle size is related to the time it takes for a particle to settle out of the atmosphere. Claiming similarity to data presented by Northrup, "settling time for particles from 10 to 100 microns require from several hours to many days" to settle out of the atmosphere. [NOR/96] Therefore, dependent upon the weather conditions at the location which releases a UO_2 particle of the size we are concerned with, the deposition of a single particle could be hundreds of miles from the source.

Extensive studies of the kinetics and mechanisms of oxidation of uranium oxides show that the process depends on multiple factors [COL/84] [RIT/81] [RIT/83] [RIT/85] [RIT/86]. Numerous studies that characterize the oxides of uranium by infrared analysis, [POW/94] [FOD/65] [FUL/83] [EID/85] [ALL/94] [GRI/91] [COL/74] [YU/88], Raman spectroscopy, [KER/73] [ALL/87] [SCH/87] [BAR/89] [ARM/89] [GRA/90], and by luminescence spectroscopy, [EKS/80] [BRI/80] [BRI/81] [PER/83] [WIN/84] [WIN/86] [KAR/82] have been accomplished, however, a single study that encompasses the three spectroscopic techniques used in this study has not been found.

Several studies have been accomplished that address the oxidation rate of uranium metal coupons [RIT/81] [RIT/83] [RIT/85] [RIT/86]. These oxidation rates are determined empirically for specific temperatures and relative humidity conditions.

It has been suggested that the transition from UO_2 to U_3O_8 progresses relatively rapidly, but that once the surface has a layer of U_3O_8, the oxidation of the particle is slowed [COL/84]. The U_3O_8 is a relatively stable molecule and has a long lifetime implying that the transition from U_3O_8 to UO_3 takes longer than the transition from UO_2 to U_3O_8. If this is the case, then a variable reaction rate will be present for the full transition from ideal starting point, UO_2 to ideal ending point, UO_3. Table 1 presents the infrared absorption peak locations for UO_3 found in the literature. Table 2 presents the infrared absorption

Table 1: UO_3 Infrared Peak Matrix

Peak (cm^{-1})	Source		
380	[ALL/94]		
425		[FOD/65]	
437	[ALL/94]		
467			[YU/88]
550		[FOD/65]	
558			[YU/88]
723			[YU/88]
726	[ALL/94]		
790			[YU/88]
800		[FOD/65]	
802	[ALL/94]		
868	[ALL/94]		
874			[YU/88]
925		[FOD/65]	
932			[YU/88]
975		[FOD/65]	

Table 2: U_3O_8 Infrared Peak Matrix

Peak (cm^{-1})	Source		
445	[ALL/94]		
465		[YU/88]	
510	[ALL/94]		
548		[YU/88]	
735			[EID/85]
737		[YU/88]	
740	[ALL/94]		
911		[YU/88]	

peak locations for U_3O_8 found in the literature.

Studies that measure this reaction rate at environmental conditions have been accomplished that use DRIFTS. Powell [POW/94] reported a UO_2 corrosion rate in both an O_2-only and air environment to

Table 3: UO_2 Infrared Peak Matrix

Peak (cm^{-1})	Source			
330		[ALL/94]		
345		[ALL/94]		
420		[ALL/94]		
430		[ALL/94]		
440				[YU/88]
450		[ALL/94]		
510		[ALL/94]		
530				[YU/88]
575	[POW/94]			
700		[ALL/94]		
1375			[FUL/83]	
1550			[FUL/83]	

be between 0.2 and 0.6 nanometers per day for a flat coupon of material. This was determined by measurement of growth in the 575 cm^{-1} peak in UO_2 coupons over time for a low relative humidity condition. They also concluded that the corrosion due to H_2O and O_2 are maintained at constant levels over wide variations in the H_2O and O_2 partial pressures. Fuller, et al. report diffuse reflectance spectra for UO_2 in hydrated and dehydrated conditions [FUL/84]. The peaks attributed to UO_2 in dehydrated conditions are located at approximately 1550, and 1350 cm-1. Table 3 presents the UO_2 infrared absorption peaks found in the literature. Fodor, et al. report UO_3 infrared spectra with absorption peaks at approximately 975 cm^{-1}, 925 cm^{-1}, 800 cm^{-1}, 550 cm^{-1}, and 425 cm^{-1} [FOD/65]. Eidson [EID/85] reports an absorption peak for UO_3 at 925 cm^{-1}, and an absorption peak for U_3O_8 at 735 cm^{-1}.

Allen [ALL/94] reports locations of peaks for several oxides of uranium, all oxides are 1% by weight in KBr. For UO_2, peaks are located at 700 cm^{-1}, 450 cm^{-1}, and 330 cm^{-1}. For U_4O_9, the peaks are located at 700 cm^{-1}, 600 cm^{-1}, 480 cm^{-1}, 400 cm^{-1}, and 330 cm^{-1}. The U_3O_8 has absorption peaks at 740 cm^{-1}, 485 cm^{-1}, and 520 cm^{-1}. U_3O_7 has absorption peaks at 510 cm^{-1}, 420 cm^{-1}, and 330 cm^{-1}. UO_3 has several absorption peaks depending on the form of the compound (α, β, γ, or δ). The α-UO_3 has peaks at 930, 890, 775, 710, 500, and 390 cm^{-1}. β-UO_3 has peaks at 965, 914, 790, 750, and 412 cm^{-1}. Peaks of 868, 802, 726, 437, and 380 cm^{-1} are found for γ-UO_3. δ-UO_3 exhibits peaks at 900, 842, and 540 cm^{-1}. Papers by Griffiths & Hubbard [GRI/91], Colmenares [COL/74], and Yu & Hansen [YU/88] show absorption peaks for UO_2 that are in agreement with the above literature.

Raman spectra have been accumulated by several researchers and suggest that UO_2 exhibits Raman peaks at 445, and 1145 cm^{-1}. Tables 4, 5, and 6 present the Raman peaks found in the literature for UO_3, U_3O_8, and UO_2, respectively. Keramidas [KER/73] reports only seeing one band at 467 cm^{-1}. Allen

Table 4: UO_3 Raman Peak Matrix

Peak (cm^{-1})	**Source**	
51		[ARM/89]
103		[ARM/89]
235		[ARM/89]
335		[ARM/89]
483		[ARM/89]
690		[ARM/89]
766		[ARM/89]
829	[BAR/89]	

Table 5: U_3O_8 Raman Peak Matrix

Peak (cm^{-1})	**Source**
238	[ALL/87]
342	[ALL/87]
408	[ALL/87]
480	[ALL/87]
752	[ALL/87]
798	[ALL/87]

Table 6: UO_2 Raman Peak Matrix

Peak (cm^{-1})	Source			
445	[KER/73]	[ALL/87]		
448				[GRA/90]
467	[KER/73]			
630				[GRA/90]
1104				[GRA/90]
1145			[SCH/87]	
1152				[GRA/90]
1156				[GRA/90]
1370			[SCH/87]	

[ALL/87] presents data for UO_2 at 445 cm^{-1}, U_4O_9 at 455 cm^{-1}, U_3O_7 at 410, 445, and 500 cm^{-1}, and U_3O_8 at 236, 342, 408, 480, 752, and 798 cm^{-1}. Schoenes [SCH/87] reports only the 1145 cm^{-1} band for the UO_2. Armstrong, et al., reports Raman peaks for γ-UO_3 at 51, 103, 235, 335, 483, 690, and 766 cm^{-1}. Graves

[GRA/90] presents spectra that was obtained from single crystals of UO_2. The peaks associated with his analysis are located at 448, 630, 1104, 1152, and 1156 cm^{-1}.

Fluorescence of the uranyl ion, uranium(VI), is presented in several works. Brittain and Perry [BRI/80] present bands centered on 510, 533, and 558 nm for two separate ligands associated with the uranyl ion and a band that shifts slightly between the two cases at 488 nm for the presented UNH complex and at 491 nm for the presented UNI complex. Table 7 presents the luminescence peak locations for UO_3 found in the literature. Brittain and Perry [BRI/81] again present work associated with the uranyl ion. In this study, they looked at the fluorescence spectrum at 77 Kelvin and found splitting in the bands that were previously reported in earlier papers. The splitting of the three; the A band, 488 nm, the B band, 510 nm,

Table 7: UO_3 Luminescence Peak Matrix

Peak (nm)	Source	
488	[BRI/80]	
491	[BRI/80]	
510	[BRI/80]	
533	[BRI/80]	[PER/84]
558	[BRI/80]	[PER/84]

and the C band, 533 nm, yields four peaks within each of these bands. The A band peaks are located at 481.5, 483.4, 487.6, and 488.4 nm. The B band peaks are located at 502.6, 504.6, 509.6, and 510.3 nm. The peaks for the C band are located at 525.4, 527.6, 532.9, and 534.0 nm. Perry, Tsao, and Brittain [PER/84] presented work with uranyl salts. Two band groups are reported with the first located around 533 nm and the second located around 558 nm. These bands vary slightly dependent upon the identity of the counterion present in the original uranyl salt used to prepare the hydrolysis product and with the nature of the base used to hydrolyze the uranyl ion. Winer, Colmenares, and Wooten [WIN/84] present preliminary results of the cathodoluminescence of uranium oxidized under a pure oxygen flow. Table 8 presents the cathodoluminescence peak location found in the literature. Cathodoluminescence is not

Table 8: UO_2 Cathodoluminescence Peak Matrix

Peak (nm)	Source	
470	[WIN/84]	[WIN/86]

always identical to photoluminescence. It is shown here because of the location of the peak. They report a cathodoluminescence peak at 470 nm (400 nm if corrected for detector response) that decreases with exposure to oxygen. They then discuss that if the oxidation were allowed to continue to reach U_4O_9, then the intensity of the fluorescence would increase since the U_4O_9 is vacancy rich for oxygen interstitials, however, they show no data.

Winer, Wooten, Colmenares, and Smith [WIN/86] present the oxidation of clean uranium exposed to oxygen at various pressures and times. They present a consistent double peak at 390 and 410 nm. Karyakin, Mel'yantseva, and Anikina [KAR/82] present data of the uranyl ion with AI-BVII phosphors. The three band structure is present in most cases, however it is usually shifted to the red in respect to the A, B, and C bands reported by Brittain and Perry [BRI/81]. In the case of a matrix of NaF+CH_3COONa, the peaks are located at 552.5, 563, and 573 nm, whereas the case of a matrix of NaF+CsCl showed no luminescence.

In the use of internal standards and benchmarks, characterization is necessary. Diamond dust is used to dilute the UO_2 powders used in this study. Cardona [CAR/94] reports a Raman peak in diamond at approximately 1320 cm^{-1}. CeO_2 is used as a benchmark for the surface deposition concerns of this study. Orel [ORE/96] states that the Raman shift of CeO_2 should be observed at between 456 cm^{-1} and 460 cm^{-1}, with a Raman peak for CeO_2 located at 459.87 cm^{-1} for a sample heated to 300 °C. Keramidas [KER/73] reports a CeO_2 Raman peak at 465 cm^{-1}. Fused silica capillaries are used for the Raman cells. Thurn and Kiefer [BAU/84] present a Raman peak at 455 cm^{-1}.

D. General Approach

In this thesis measurements of the oxidation of standard UO_2 particles in several controlled environments are undertaken. The goal is to determine if the rate of oxidation under typical environmental conditions will actually be useful for the dating of particles. If significant changes occur over time periods ranging from days to years, then oxidation will be a useful tool for this application. The data collected has been tabulated and looked at to determine if the three techniques are viable methods for measuring the oxidation of UO_2. This is determined by looking at characteristic peaks in each of the

techniques for the uranium oxides. Also, characteristic bands for carbonates (infrared peaks in range from 1050 to 1300 cm^{-1}), hydroxides (infrared peaks in ranges from 1500 to 1700 cm^{-1} and 3200 to 3650 cm^{-1}), and nitrates (infrared peaks in ranges from 1300 to 1370 cm^{-1} an 1500 to 1570 cm^{-1}) are tracked.[SKO/92] The relative intensities are compared. If a certain peak diminishes in intensity and a peak corresponding to another compound increases, then the degree to which the relative change occurs will determine the suitability of that technique.

Cerium was chosen as an actinide simulant for surface deposition concerns for two basic reasons. The first is cerium dioxide is Raman active, IR active and fluoresces. Second, and more importantly, it is a heavy, non-toxic, non-radioactive, non-hazardous material. There are no health risks associated to working with cerium oxides that have been found. This allows the flexibility to test the procedures for the uranium studies and adhere to the ALARA concept (ALARA is radiation exposure As Low As Reasonably Achievable). With the size of particles used, 1 to 20 micron, precautions are taken against inhalation of the material in the form of respirators, goggles, and gloves worn at all times.

II. Theory

A. Uranium Chemistry

Uranium was first discovered in the mineral of pitchblende by the Curies. Since its discovery, it has become one of the most important elements for nuclear reaction concerns. It was utilized as the fuel, pit, for the worlds first nuclear weapon detonation in 1944. It has also become a primary component of nuclear fuels for several types of nuclear power reactors around the world. There has been much study of uranium and its compounds for these purposes since the early 1940s. Through these studies, uranium oxides emerged as a viable compound to be used as a fuel for nuclear reactors. It is a ceramic that can be formed into pellets and placed into fuel pins. It doesn't change its physical characteristics under reactor conditions to the extent that uranium metal does. Uranium metal expands tremendously under irradiation and heat, whereas, uranium dioxide, deforms negligibly under the same conditions.

What happens to the UO_2 compound once it is exposed to the atmosphere? Several empirical studies have been accomplished, namely by Ritchie, but few of these studies limit themselves to only atmospheric conditions. The actual phase of the uranium oxide is dependent upon several conditions, temperature, pressure, O/U ratio, etc... A phase diagram that relates temperature to U/O ratio with the phases present is shown in figure 1. The region of the phase diagram that we are concerned with is between 0 and 200 degrees centigrade. We are beginning with a O/U ratio of 2.0. We are adding oxygen to the system in the form of O_2 and CO_2 gases. The O/U ratio increases and we expect the material to oxidize and take on the forms of the O/U system described in the temperature region. We are not doing anything to our system to heat above 200 degrees centigrade on the phase diagram. Neither are we cooling the system to below 0 degrees centigrade.

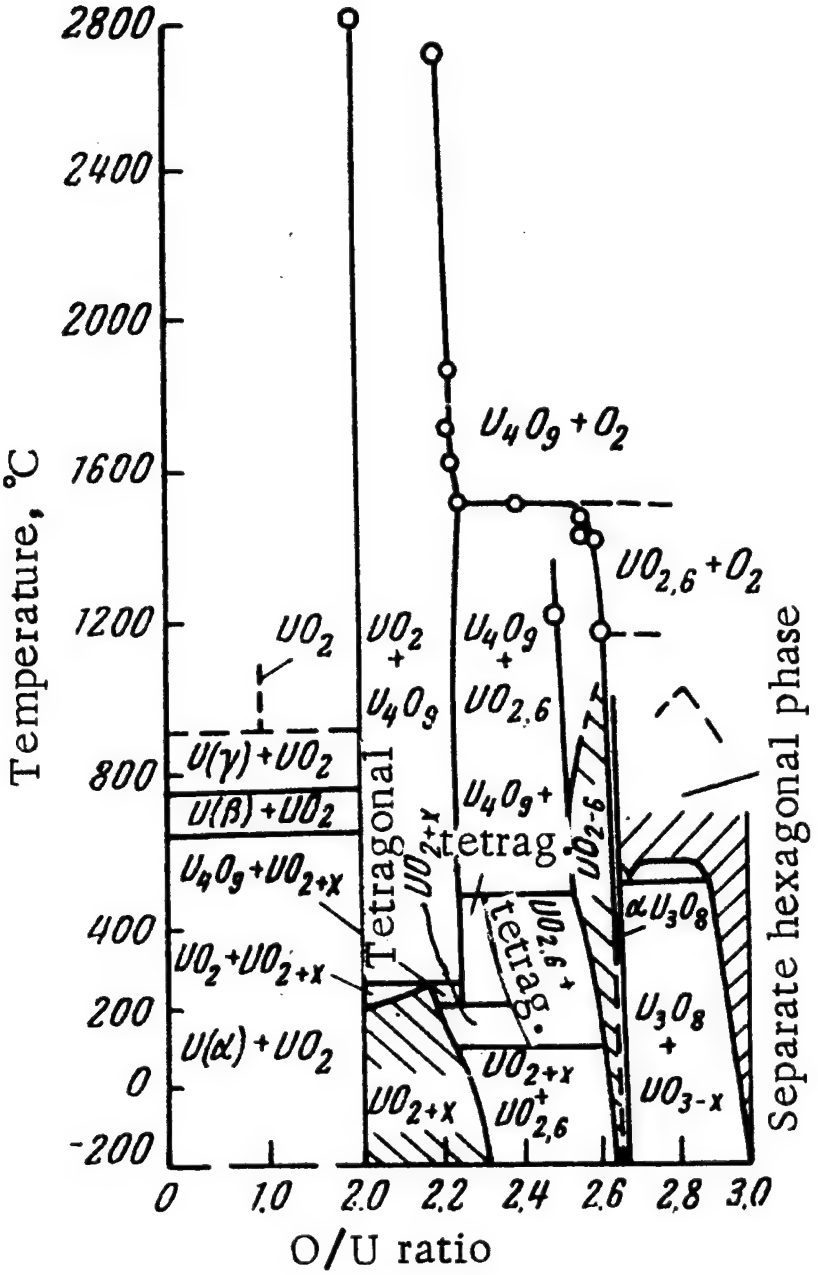

Figure 1: Phase Diagram of Uranium-Oxygen System [SAM/73]

B. Photoluminescence Spectroscopy

The following discussion on photoluminescence spectroscopy is taken from Skoog & Leary [SKO/92]. The discussion portrays a general approach to photoluminescence and the processes involved.

Molecular species exhibit fluorescence at wavelengths that are typically above that of the exciting

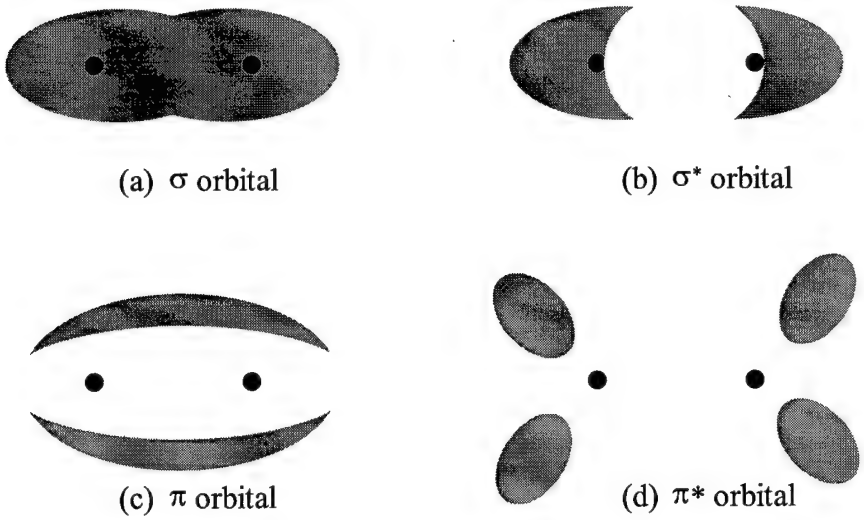

Figure 2: Charge Distributions of Pi and Sigma Orbitals

radiation. This is termed the Stokes shift. Fluorescence and phosphorescence can be described by molecular orbital transitions. Absorbing species contain three types of electrons; n, σ, and π. Each type of electron is associated with a molecular orbital. The σ orbital is the molecular orbital associated with single bonds. The double bond contains two types of orbitals; a σ orbital corresponding to one pair of bound electrons and a π orbital corresponding to the other pair. The π orbitals are formed by parallel overlapping of atomic p orbitals. The n electrons are those that are nonbonding in the molecule. Figure 2 shows the charge distributions associated with the σ and π orbitals in both the low-energy bonding molecular orbitals, (a) and (c), and the high-energy antibonding molecular orbitals, (b) and (d).

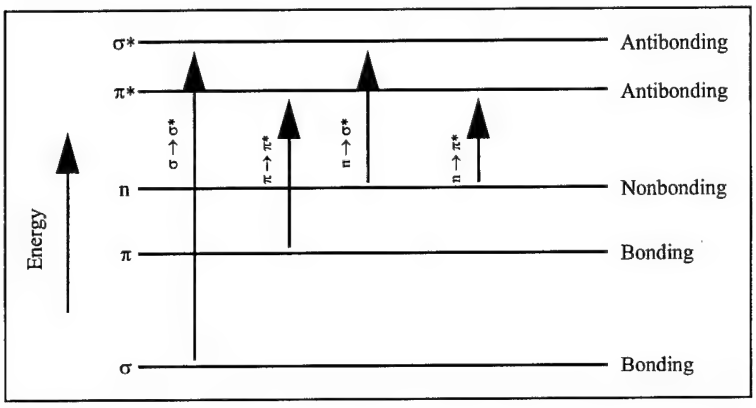

Figure 3: Electronic molecular energy levels

There are four possible transitions that can take place between the energy levels of the molecular orbitals. They are: $\pi \rightarrow \pi^*$, $n \rightarrow \pi^*$, $\acute{n} \rightarrow \sigma^*$, and $\sigma \rightarrow \sigma^*$. Figure 3 shows the possible transitions between molecular energy levels. As pictured in figure 2, the $\sigma \rightarrow \sigma^*$ transition requires the most energy. The transition from the bonding σ orbital to the corresponding antibonding, σ^*, orbital is accomplished by absorption of radiation. The energy required corresponds to radiation with wavelengths of less than 150 nm, in the vacuum ultraviolet region. Unless great pains are taken to eliminate atmospheric absorption, this transition will not be seen. The $n \rightarrow \sigma^*$ transition requires less energy than the $\sigma \rightarrow \sigma^*$ transition and can be brought about by energies associated with radiation with wavelengths from 150 to 250 nm. Again, unless great pains are taken to eliminate atmospheric absorption, these transitions will not be seen. Most applications of absorption spectroscopy are based on the $\pi \rightarrow \pi^*$ and $n \rightarrow \pi^*$ transitions because the energies required for these transition are in the 300 to 700 nm region of the spectrum. This is very convenient because there is little atmospheric absorption in this region. If the sample is in an aqueous form, the difference between the two transitions can be observed by changing the solvent to one of higher polarity. A blue shift will normally occur if the peak location is due to a $n \rightarrow \pi^*$ transition. If the peak location is due to the $\pi \rightarrow \pi^*$ transition, there will typically be a red shift.

For the lanthanide and actinide series, the absorption is from electronic transitions of the 4f and 5f electrons, respectively. A distinct difference relative to most organic and inorganic absorbers is that the

spectra of lanthanides and actinides are generally narrow and well-defined. They are relatively unaffected by the type of ligand that the metal ion is associated with.

The difference between fluorescence and phosphorescence can be explained with a discussion of electron spin and singlet and triplet excited states. The Pauli exclusion principle states that no two electrons in the same atom can have the same set of quantum numbers. This limits the number of electrons in an orbital to two, which must have opposed spins. If this is the case, then the spins are said to be paired. Because of spin pairing, most molecular species have no net magnetic field and are classified as diamagnetic, repelled by permanent magnetic fields. Those molecular species that are known as free radicals have one or more unpaired electrons. They then have net magnetic moment and are attracted to magnetic fields. These are called paramagnetic.

A molecular electron state in which all electrons are paired is called a singlet state. No splitting of the energy levels is observed when the molecule is exposed to a magnetic field (neglecting nuclear spin). A free radical's ground state is called a doublet because the unpaired electron can assume two orientations in a magnetic field with slightly different energies imparted to the system. When one electron of a pair in a molecule is excited to a higher energy level, a singlet or triplet state is permitted. In an excited singlet

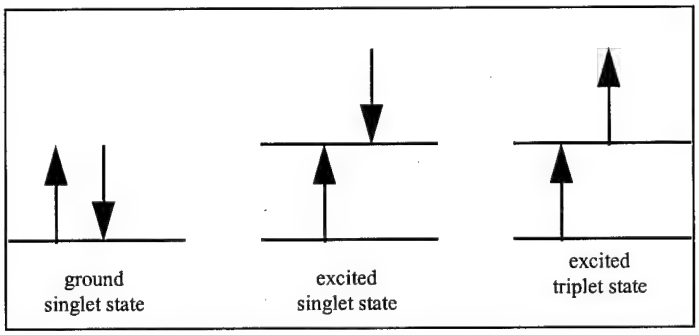

Figure 4: Singlet and Triplet Molecular States

state, the excited electron stays paired with the ground state electron. In the excited triplet state the excited electron is no longer paired with the ground state electron, thereby yielding parallel spins. Figure 4 shows a graphical representation of the three states.

The properties of a molecule in the excited triplet state differ significantly from those in the excited singlet state. One obvious difference is that the excited triplet state is paramagnetic while the

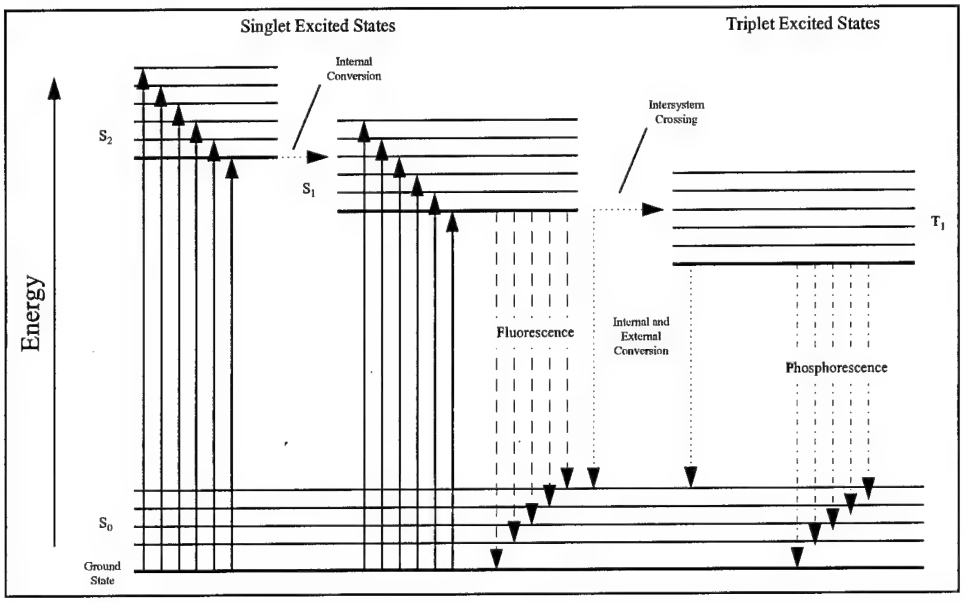

Figure 5: Partial Energy Diagram for a Photoluminescent System (vibrational relaxations not pictured)

excited singlet state is diamagnetic. A difference of more importance, for the purpose of this thesis, is the fact that the singlet/triplet transition (or the reverse transition) is much less probable than a singlet/singlet transition. Therefore, the average lifetime of an excited triplet state is on the order of 10^{-4} to several seconds. The average lifetime of the excited singlet state is roughly 10^{-5} to 10^{-8} seconds. Figure 5 shows a simplified energy diagram for a photoluminescent system [SKO/92]. The absorption of energy is pictured by the solid ascending arrows. Fluorescence is shown as occurring in a very short time frame, roughly 10^{-5} to 10^{-8} seconds. Phosphorescence is shown as occurring over a longer time frame, 10^{-4} to several seconds. The extra time is due to the intersystem crossing that takes the molecule from an excited singlet state to an excited triplet state. The ground electronic state is shown as S_0, while S_1, and S_2 represent excited molecular energy levels.

C. Infrared Spectroscopy

Generally, infrared radiation does not possess the energy necessary to cause electronic transitions that are associated with fluorescence and phosphorescence. Due to this fact, infrared is generally limited to interactions with molecular species with small energy differences between rotational and vibrational energy states.

For a molecule to absorb the infrared radiation, it must undergo a net change in dipole moment related to the vibrational or rotational motion. This must occur if the incident radiation is to effect the amplitude of one of the motions of the molecule. As an example, the hydrogen chloride molecule, HCl, does not have a symmetric charge distribution. The chlorine has a higher electron density than does the hydrogen. Therefore, the hydrogen chloride has a large dipole moment and is said to be polar. The dipole moment is determined by the difference in charge and the distance between the centers of those charges. As an HCl molecule vibrates, the dipole moment undergoes regular fluctuations and a field arises that can interact with the incident radiation's associated electrical field. If the frequency of the incident radiation exactly matches a natural vibrational frequency of the molecule, a net transfer of energy occurs and results in a change in the amplitude of the molecular vibration. Similarly, the rotation of asymmetric molecules around their centers of mass will produce a periodic dipole fluctuation which can interact with incident infrared radiation. On the other hand, an oxygen molecule, O_2, is symmetric and has a uniform electron distribution around the molecule. There is no dipole moment present and therefore, it cannot absorb in the infrared.

Two types of transitions occur in this regime, vibrational and rotational. The energy required to effect a rotational change corresponds to wavelengths larger than 100 microns. Due to the quantization of the energy levels, the absorption is well characterized by sharp spectral lines. The vibrational levels are also quantized, and for most molecules, the energy differences between levels resides in the mid infrared region. Table 9 gives some accepted ranges for infrared classifications.

Table 9: Infrared Spectral Regions

	Wavelength (λ)		Wavenumber (cm^{-1})		Frequency (Hz)	
Region	**Min (μm)**	**Max (μm)**	**Min (cm^{-1})**	**Max (cm^{-1})**	**Min (Hz)**	**Max (Hz)**
Near	0.78	2.5	12800	4000	3.8×10^{14}	1.2×10^{14}
Middle	2.5	50	4000	200	1.2×10^{14}	6.0×10^{12}
Far	50	1000	200	10	6.0×10^{12}	3.0×10^{11}
Most Used	2.5	15	4000	670	1.2×10^{14}	2.0×10^{13}

The relative positions of atoms in a molecule are not exactly fixed, but rather fluctuate with all of the vibrations that are occurring. For a simple diatomic or triatomic molecule it is relatively easy to define the number and nature of those vibrations and relate them to specific energies of absorption. An analysis of a molecule containing several atoms is very difficult due to the large numbers of vibrating centers and interactions between multiple centers that must be taken into account.

Vibrations fall into two general categories, stretching and bending. Stretching vibrations involve continuous changes in the interatomic distance along the axis of the bond and can either be symmetric or asymmetric. Bending vibrations involve changes in the angles between bonds in the molecule. There are four types of bending vibrations: scissoring, rocking, wagging, and twisting. Figure 6 shows the schematics of the six basic vibrations just mentioned.

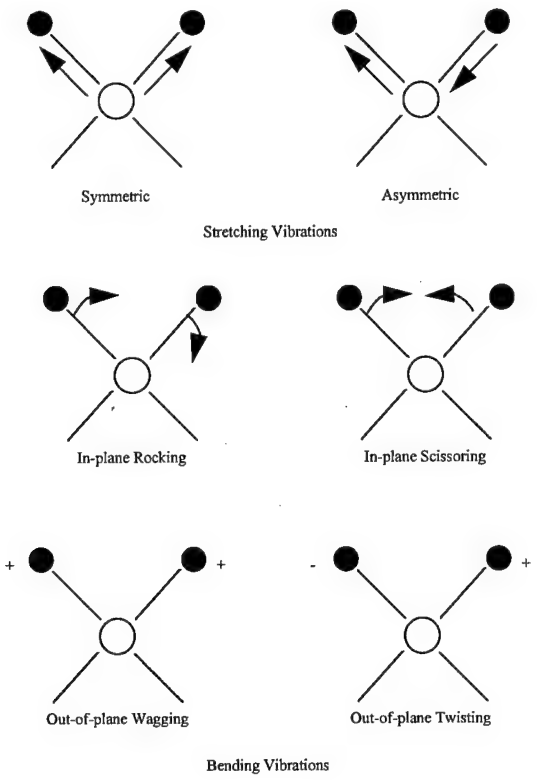

Figure 6: Types of Molecular Vibrations (+/- indicate into/out of page)

Classical equations relating the stretching of a bond to harmonic oscillator motion provide a reasonable approximation. It is necessary to utilize a quantum treatment of the vibrations in order to characterize them more precisely. It is possible to extend the often used harmonic oscillator concept in a development of the wave equations of quantum mechanics. Solutions to those equations for potential energy are of the form

$$E = (v + \frac{1}{2})\frac{h}{2\pi}\sqrt{\frac{k}{\mu}} \qquad (1)$$

where h is Planck's constant and v is the vibrational quantum number. The vibrational quantum number can take on values of only positive integers (including zero). Making a substitution in the above equation yields

$$E = (v + \frac{1}{2})h\nu_m \tag{2}$$

where

$$\nu_m = \frac{1}{2\pi}\sqrt{\frac{k}{\mu}}. \tag{3}$$

where ν_m is the vibrational frequency of the mechanical model. Let us assume that transitions in the vibrational levels can be brought about by radiation, whose energy must be identical to the difference, ΔE, between energy levels. This difference between any two adjacent levels is identical. This is because v can only take on integer values. There can only be a transition if $\Delta v = \pm 1$. Since the vibrational levels are equally spaced, there should only be one absorption peak observed for each molecular vibration. This is mostly true, however, a more thorough quantum mechanical treatment allows for the possibility of anharmonic solutions that deviate with varying degrees from the harmonic oscillator described above. However, at low potential energies, the two models are almost identical, which allows usage of the harmonic oscillator approximations. The region where the harmonic oscillator approximation is not very accurate is at high vibrational quantum numbers. Here the anharmonic approximations must be used. This is because at higher vibrational quantum numbers, the energy difference gets smaller and smaller. In fact, if the vibrational quantum number is large enough, transitions of $\Delta v = \pm 2$ and $\Delta v = \pm 3$ can be observed. Such transitions are responsible for the overtones that may be observed at approximately two or three times the frequency of the fundamental line. Vibrational spectra can be complicated even further by the interaction of vibrations in a molecule giving lines that are approximately the sums or differences of their fundamental lines.

A drawback to the usage of infrared spectroscopy occurs if the sample must be contained in a sealed cell. To get the radiation into the cell to the sample, a window must be used. At the present time, the windows that are commonly used, KBr, KRS-5, and Diamond, either react with the environment, or are prohibitively expensive.

D. Raman Scattering

A complementary technique to infrared, Raman spectroscopy arises from the same type of quantized vibrational changes that are associated with infrared absorption. Thus the difference in wavelength between the incident radiation and the scattered radiation corresponds to wavelengths in the mid-infrared region of the spectrum. The Raman scattering spectrum is similar to that of the infrared absorption spectrum, however, there are enough differences between the kinds of groups that are infrared active and Raman active, to make the techniques complementary. An important advantage of Raman spectra over infrared is that water does not cause interference. In fact, Raman spectra can be obtained from aqueous solutions. Also, glass or quartz cells can be utilized, avoiding the inconvenience of atmospherically unstable windows required for infrared. Despite these advantages, Raman spectroscopy was not widely used until the 1960s, when lasers became available. The laser makes the spectra much easier to obtain.

Raman spectra are obtained by irradiating a sample with a laser source of visible or near-infrared radiation . During irradiation, the spectrum of the scattered radiation is measured at some angle, usually 90 degrees, with a suitable spectrometer. At the very most, the intensities of the Raman lines are 1.0×10^{-5} that of the intensity of the source. As a consequence of the low intensities, the detection and measurement of Raman spectra are difficult. However, with the use of a near-infrared laser and Fourier transform techniques, the spectra are becoming easier to obtain. A problem that still persists in the study of Raman spectroscopy, however, is that fluorescence may cause interference if the exciting laser wavelength is at an absorption peak in the sample. Rayleigh scattering, incident radiation that is scattered with no change in wavelength, is usually removed from the spectra through the use of a notch filter which excludes transmission of the exciting wavelength.

Superficially, the appearance of spectral lines at longer wavelengths is analogous to the Stokes shifts found in fluorescence. For this reason, negative Raman shifts are referred to Stokes shifts. Shifts towards higher energies, shorter wavelengths, are referred to as anti-Stokes shifts. The anti-Stokes lines are much less intense than the Stokes lines. If fluorescence from the sample overwhelms the Raman Stokes

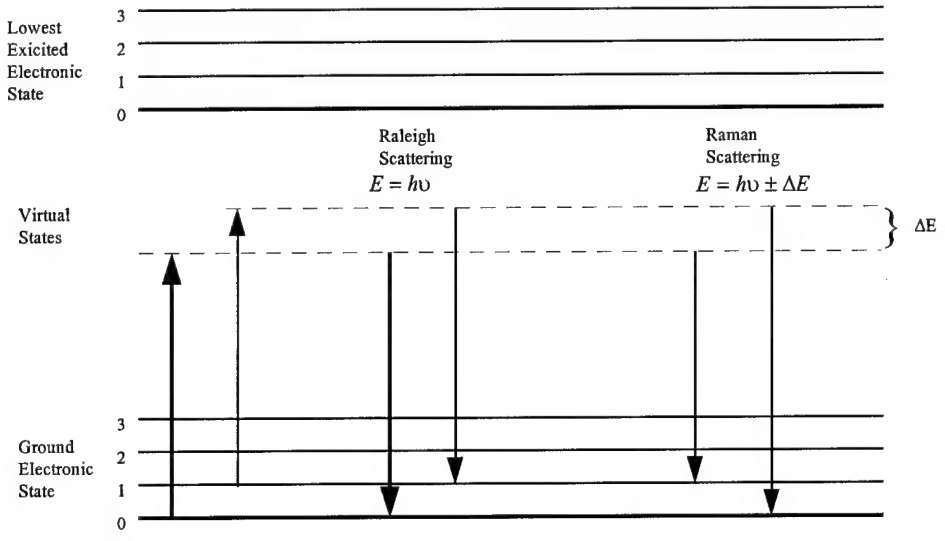

Figure 7: Origin of Rayleigh and Raman Scattering

shifts, then the lines associated with the anti-Stokes shifts can be used for analysis since they are unaffected by fluorescence. Even though the term Stokes shift is applied to the Raman shifts, the process that produces the Raman shift is not associated with the fluorescence process. Figure 7 shows how the Rayleigh and Raman shifts come about. The states shown are molecular energy states. It is important to note that the process of Raman scattering is not quantized; thus, depending on the frequency of radiation from the source, the energy of the molecule can assume any number of virtual states between the ground electronic and the first electronic state as shown in the diagram. The heavy arrows are the most probable transitions. Note that no energy is lost in Rayleigh scattering, therefore it is an elastic collision. The Stokes and anti-Stokes lines of the Raman scatter differ from the Rayleigh radiation by frequencies corresponding to $\pm \Delta E$, the energy of the first vibrational level of the ground state. Note that if the bond were infrared active, the energy of its absorption would also be ΔE. It should also be noted that the ratio of

anti-Stokes to Stokes intensities will increase with temperature, as there will be more molecules in the first vibrational state as the temperature increases.

Raman and Rayleigh scattering can be described with a wave model. The following derivation is taken directly from Skoog and Leary [SKO/92] Chapter 13. If we are to assume that a beam of radiation is incident upon an analyte with frequency ν_{ex}, then the electric field, *E,* of this radiation can be described by the equation:

$$E = E_0 \cos(2\pi \ \nu_{ex} t) \tag{4}$$

where E_0 is the amplitude of the wave. When the electric field of the radiation interacts with the electron cloud of an analyte bond, it induces a dipole moment, *m*, in the bond that is given by:

$$m = \alpha \cdot E = \alpha \cdot E_0 \cos(2\pi \ \nu_{ex} t) \tag{5}$$

where α is a proportionality constant called the polarizability of the bond. This constant is a measure of the deformability of the bond in an electric field.

In order to be Raman active, the polarizability of the bond must vary as a function of the distance between nuclei according to the equation

$$\alpha = \alpha_0 + (r - r_{eq})\left(\frac{\partial \alpha}{\partial \ r}\right) \tag{6}$$

where α_0 is the polarizability of the bond at the equilibrium internuclear distance r_{eq} and r is the internuclear separation at any instant. The change in the internuclear separation varies with the frequency of the vibration ν_v as given by

$$r - r_{eq} = r_m \cos(2\pi \ \nu_v t) \tag{7}$$

where r_m is the maximum internuclear separation relative to the equilibrium position. Substituting Equation 7 into Equation 6, we obtain

$$\alpha = \alpha_0 + \left(\frac{\partial \alpha}{\partial r}\right) r_m \cos(2\pi \nu_v t) \tag{8}$$

We can then substitute Equation 8 into Equation 5 and find an expression for m, the induced dipole moment

$$m = \alpha_0 E_0 \cos(2\pi \nu_{ex} t) + E_0 r_m \left(\frac{\partial \alpha}{\partial r}\right) \cos(2\pi \nu_v t) \cos(2\pi \nu_{ex} t) \tag{9}$$

Recall from trigonometry that

$$\cos(x)\cos(y) = \frac{[\cos(x+y) + \cos(x-y)]}{2}$$

applying this identity to Equation 9 gives

$$\begin{aligned} m &= \alpha_0 E_0 \cos(2\pi \nu_{ex} t) \\ &+ \frac{E_0}{2} r_m \left(\frac{\partial \alpha}{\partial r}\right) \cos[2\pi (\nu_{ex} - \nu_v) t] \\ &+ \frac{E_0}{2} r_m \left(\frac{\partial \alpha}{\partial r}\right) \cos[2\pi (\nu_{ex} + \nu_v) t] \end{aligned} \tag{10}$$

The first term in this equation represents the Rayleigh scattering which occurs at the excitation frequency, ν_{ex}. The second and third terms represent the Stokes and anti-Stokes scattering of Raman scattering. Raman scattering requires that the polarizability of a bond varies as a function of distance, that is $\left(\partial\alpha/\partial r\right) > 0$.

III. Experiment

A. Equipment

Several challenges present themselves due to the fact that we are dealing with radioactive powders. The entire weathering apparatus and the cells in which the samples were contained were designed for the purpose of allowing environmental conditions to mix with the sample while containing the fine particulate samples. The apparatus has four chambers for a variety of temperature and UV exposure conditions. There are two room temperature chambers, one with a UV lamp and one without. The other two chambers are maintained at elevated temperatures, 40° C and 130° C. Figure A-1, Appendix A, shows a schematic of the apparatus design. The cell for the infrared diffuse reflectance measurements is more complicated. It must be able to contain the particulates, pass infrared radiation, and pass UV radiation. A drawing of this cell design is pictured in figure A-2 of Appendix A. The cells that were used for the Raman and the luminescence samples are fused silica capillary tubes with 0.5 micron frits attached to both ends, drawing is shown in figure A-3 of Appendix A. The frits allow for exposure to the desired environmental conditions while containing the powders (powder sizes are larger than 1.0 micron).

Within the apparatus, there must be a way for the air to obtain the desired relative humidity levels. This is accomplished with a combination of a gravity fed drip system and a saturated salt solution. De-ionized (De-I) water is dripped into a container and evaporated into the air that is moving through the container, then this pre-wetted air is bubbled through a saturated NaCl solution to obtain approximately 76% relative humidity at 25° C [LID/95]. The De-I water is fed from a reservoir which can be refilled without disturbing the system. The reservoir is situated so that no external gases can dissolve into the De-I water throughout the experiment. The only gas that can possibly dissolve into the water, by design, is nitrogen, an inert gas used in our experiment.

The temperature controls for the elevated temperature chambers are calibrated to a temperature variance of ±2.0° C. A baseline is established with the UO_2, U_3O_8, UO_3, and the CeO_2 prior to any environmental exposure. These baselines are needed for each technique (IR, Raman, Luminescence).

Also, the drip rate of the pre-wetting system is set so as not to saturate the air prior to bubbling through the salt solution. The salt solution container is required to maintain a saturated condition throughout the course of the exposure.

All samples are prepared in a glove box containing a nitrogen environment. Figure 8 shows a schematic of glove box with the airlock. The airlock is a twelve inch diameter cylinder. This will contain the uranium should any accidents occur, as well as limit the time for the cells to reach equilibrium in their respective environments. As a rule, any time that a powder is to be outside of a cell or the containers that they are stored in, they must be inside of the glove box.

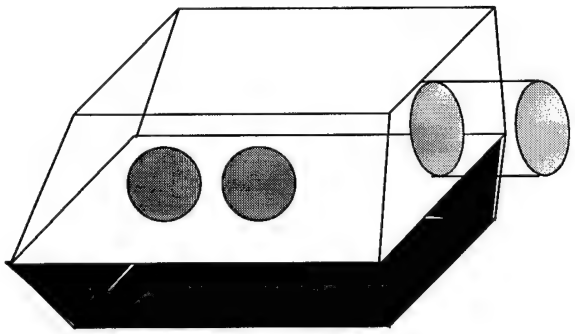

Figure 8: Glove Box Containment Chamber

The apparatus is tested with a nitrogen flow to ensure that all components are connected properly and that there are no leaks in the system. CeO_2 is used for all simulated test runs in the cells and in the system as a whole. This will be done prior to use of any uranium. A materials and chemicals list for the weathering apparatus and the exposure cells is found in appendix A.

1. Off-the-Shelf Equipment

The majority of the off-the-shelf equipment used was in the form of spectrometers or accessories to the spectrometers. A list of the major equipment used for each technique, as well as the accessories required, is shown in Table 2. The Farrand Spectrofluorometer and the ISA/Spex FL3 systems are

Table 10: Commercial Spectrometers and Accessories Used

Technique	Equipment	Accessories
Luminescence	Farrand Spectrofluorometer	None
Luminescence	ISA/Spex Fluorolog 3 FL3-11	None
Luminescence	ISA/Spex Fluorolog 3 FL3-22	None
DRIFTS	Bomem MB Series Spectrometer	Graseby Diffuse Reflectance Selector
FT-Raman	Bomem MB Series Spectrometer	Bomem Raman Accessory with Nd:YAG Laser
Visible Raman	ISA/Spex Fluorolog 3 FL3-11	Argon Ion Laser (488 nm)
Visible Raman	ISA/Spex Fluorolog 3 FL3-22	Argon Ion Laser (488 nm)

monochrometer systems, while the Bomem MB Series system is a Fourier transform system. A monochrometer system scans through the spectrum of interest sequentially, sitting at a single wavelength for a given amount of time. Figure 9 is a schematic diagram of the ISA/Spex FL3-11 monochrometer system. A Fourier transform system analyzes the whole spectrum at once and corrects for a moving mirror

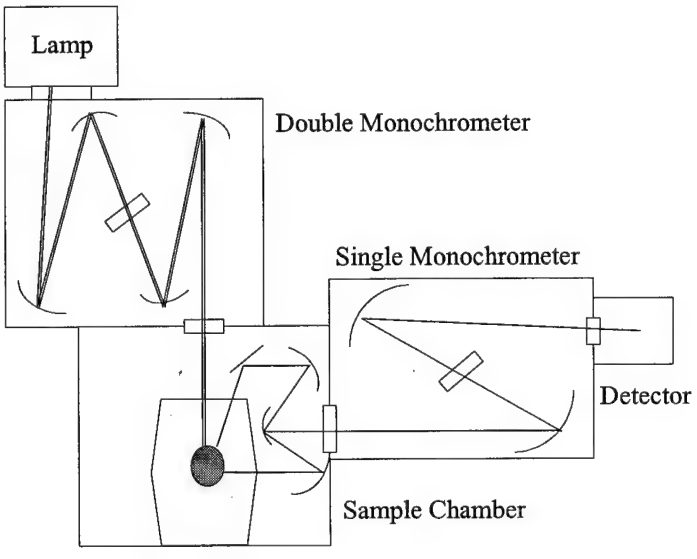

Figure 9: Schematic of ISA/Spex FL3-11 System

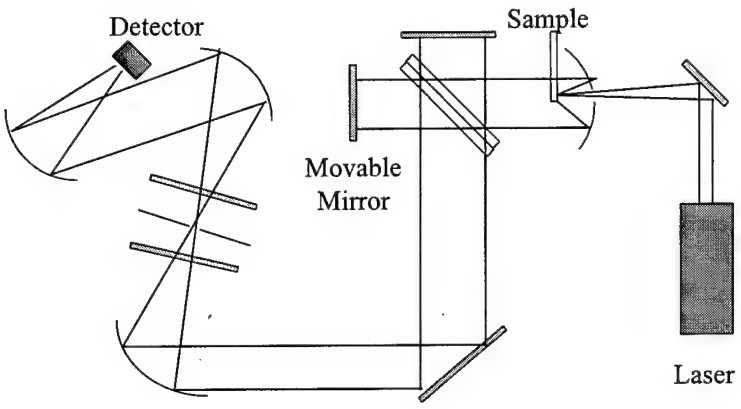

Figure 10: Schematic of a Near IR Fourier Transform Spectrometer

in the system. A Fourier transform system is somewhat different as it employs a movable mirror that is moved in a controlled manner producing an interferogram. The spectrum is obtained by taking the Fourier transform of the interferogram received at the detector. Figure 10 is a schematic of a Fourier transform system.

2. Designed Equipment

Not all of the equipment used for this experiment was available off the shelf. The weathering apparatus was discussed earlier in this chapter, as were the DRIFTS cells and the luminescence/Raman cells. In order to fill the capillary cells with the sample material, a Teflon funnel was fashioned to allow for filling the cells without loss of material.

Figure 11 is a schematic of the weathering apparatus used in this study. Each bottle of gas serves two lines, a dry line and a constant humidity line. The volume of the apparatus that is exposed to the gas flow, is approximately 0.924 liters. With an exchange rate of 1.0 liter per hour, or exchanging the gas volume once every two hours, each bottle of gas is expected to last for 300 days. For the controlled humidity lines, a relative humidity of 65% is desired to be maintained in the pre-wetting chambers. To accomplish this, 5.52 ml/hr must be absorbed from the pre-wetting chambers. The entire weathering apparatus is placed in a fume hood. This is as a precaution against contamination of the area in the event of uranium oxides escaping from the system. The gas compositions of each line are shown in Table 11.

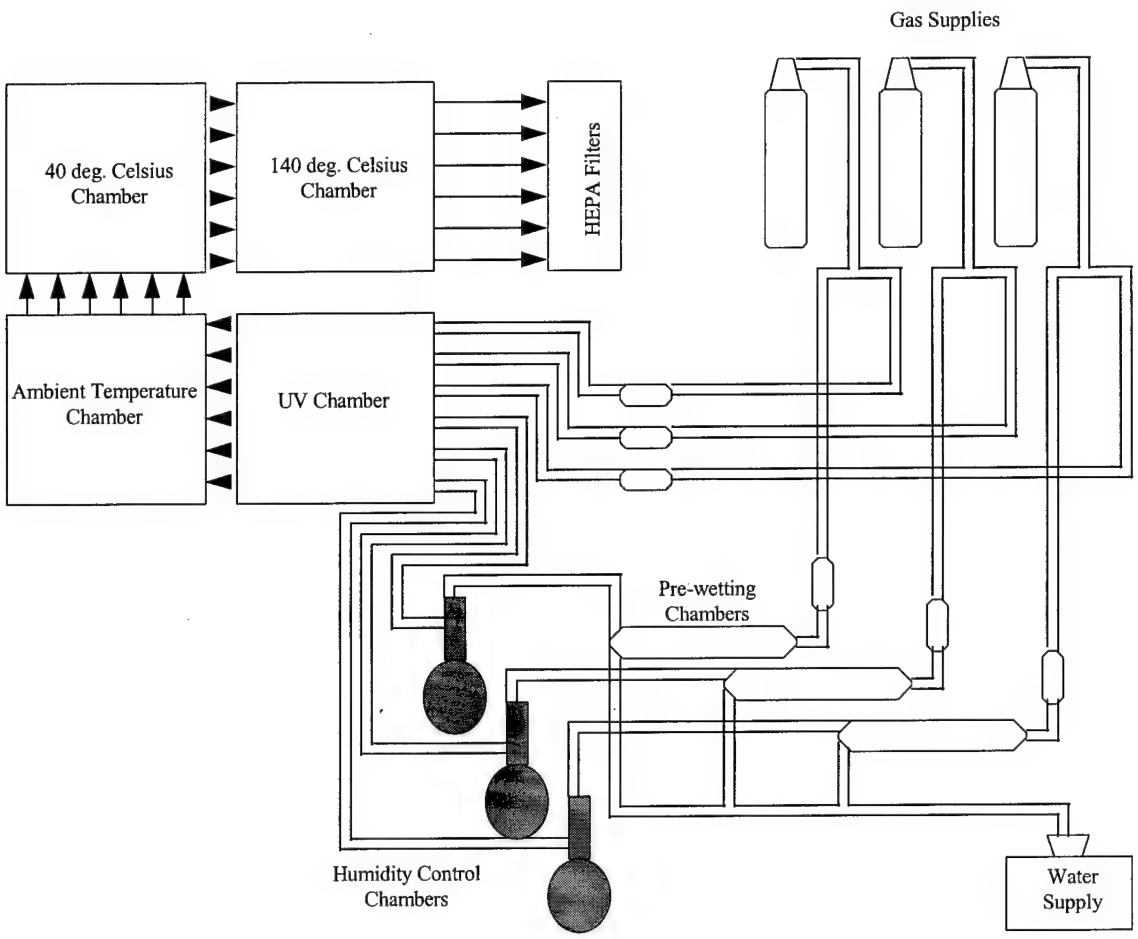

Figure 11: Six-Line Weathering Apparatus Schematic

Table 11: Gas and Humidity Composition

Gas Line	Humidity (@ 398 K)	Oxygen	Carbon Dioxide	Nitrogen
1	Dry	21%		balance
2	Dry	21%	0.03%	balance
3	Dry	21%	0.15%	balance
4	76% RH	21%		balance
5	76% RH	21%	0.03%	balance
6	76% RH	21%	0.15%	balance

To determine the values stated above, Table 12 shows the parameters used for the calculations using the ideal gas law:

$$PV = \frac{mRT}{(MW)} \tag{11}$$

where:

P = Partial Pressure of H_2O at 65% relative humidity

= Volume of air to be exchanged

m = mass of water to be absorbed

R = Universal Gas Constant

T = Temperature in Kelvin

MW = Molecular Weight of H_2O

Table 12: Parameter List for Bottle Lifetimes and Pre-Wetting Drip Rates

Parameter	Value	Units
Volume (bottle)	$7.55*10^3$	liters
Volume (line)	924.0	cm^3
Gas Exchange Rate (per line)	0.50	liters/hour
Pressure, P_e, (H_2O)	19.0	Torr
Relative Humidity (@ 25°C)	65	%
Partial Pressure (H_2O)	0.01625	atmospheres
Temperature	25	°C
Molecular Weight (H_2O)	18	g/mole
R (gas constant)	0.0821	liter atmos/K mole
Mass Rate (H_2O required)	5.52	milligrams/hour

The partial pressure of H_2O is determined by formula 12 as obtained from [LID/95]. The formula is:

$$P = P_e \times \frac{RH_d}{100\%} \tag{12}$$

where:

P_e = Pressure of H_2O

RH_d = Desired Relative Humidity

The drip rate into each pre-wetting chamber of the apparatus was controlled by a titration tube with a stopcock. The titration tubes were continually fed from a 20 liter reservoir of De-I water. Once an acceptable flow rate was established, it was monitored to ensure that the decrease of water in the reservoir did not affect the flow rate over a period of 18 hours. A four-line peristaltic pump has been obtained to replace the titration tubes, however it will not be placed into the apparatus until more gases can be obtained and a gas bottle changeover is performed. The relative humidity level of the gas leaving the pre-wetting chamber was chosen to be close, but below the salt solution maintained relative humidity in the wet lines of the apparatus. The salt solution used in the apparatus is a saturated NaCl solution in De-I water. This solution maintains a relative humidity of 76% at 25°C.

The two elevated temperature requirements were chosen to give a real world high temperature condition (40°C) and an accelerated weathering condition (140°C). The error allowed in the temperature controls is due to the combination of transformers, heat tape, and exposure chambers. The combination of the transformer and heat tape allows for control to approximately 0.5°C, however the chamber in which these temperatures are maintained is a large heat sink (stainless steel box), therefore, tolerances were given a factor of four margin.

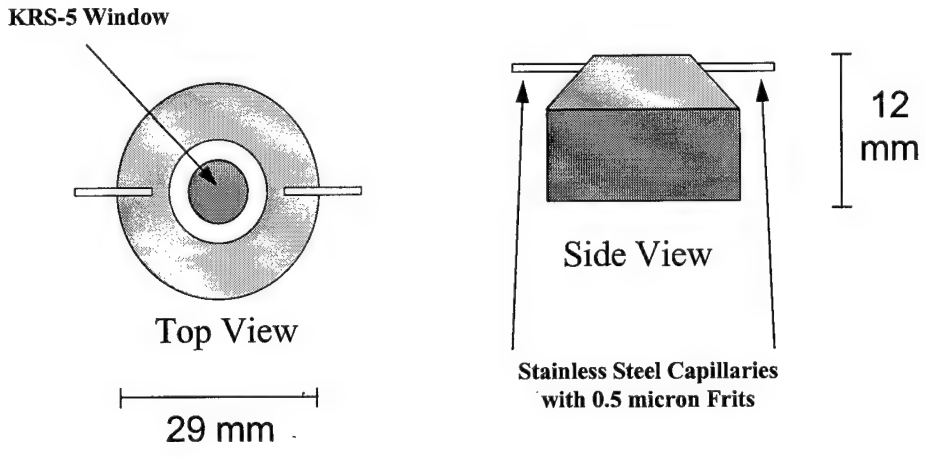

Figure 12: DRIFTS Sample Cell

The design of the DRIFTS cell for the Graseby Selector is similar in concept to the weathering apparatus. It must allow air flow, have an IR transparent window, and provide containment of the uranium oxides. The cell accomplishes this by having the air flow through 0.5 micron frits (filters designed for use in HPLC, high pressure liquid chromatography) with a KRS-5 (TlBr•TlI) window. A drawing of the infrared cell is shown in figure 12. The window is affixed to the stainless steel cell using a NASA approved, high vacuum epoxy produced by Masterbond, Inc. A quartz window can be affixed to the underside of the cell to allow for UV transmission into the sample, or a plug of stainless steel or aluminum can be placed there if no such exposure is required. The armatures on the sides are stainless steel capillary tubes that lead to the sample. There is a frit on each tube adjacent to the sample.

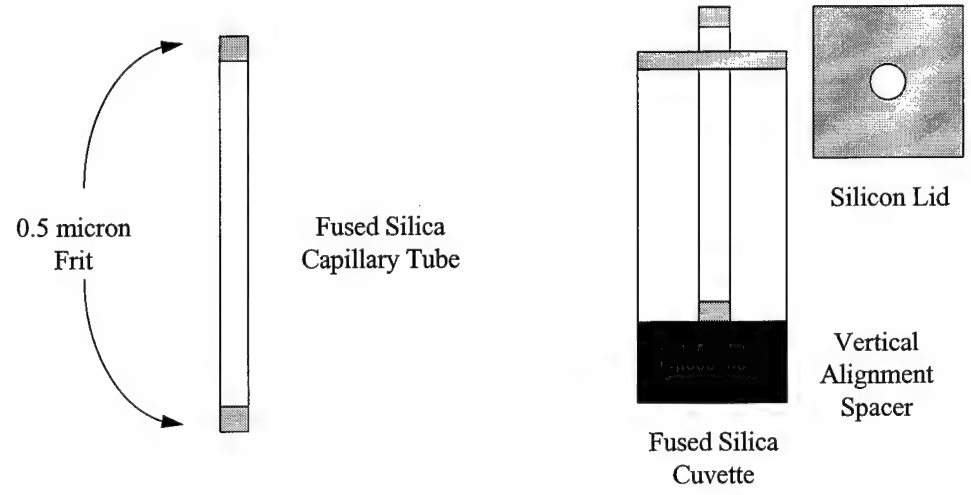

Figure 13: Luminescence Cell and Cell Holder

The cells for the Raman and luminescence are fused silica capillary tubes with 0.5 micron frits affixed to the ends. Again, the affixing is accomplished with Master Bond's high vacuum epoxy. These cells are only filled to half capacity to allow for air flow within the cell. The frits will let air pass through, but will not allow the particles to escape the cell. A drawing of the luminescence cell, and the holder which positions the cell in the FL3-11 system, is shown in figure 13.

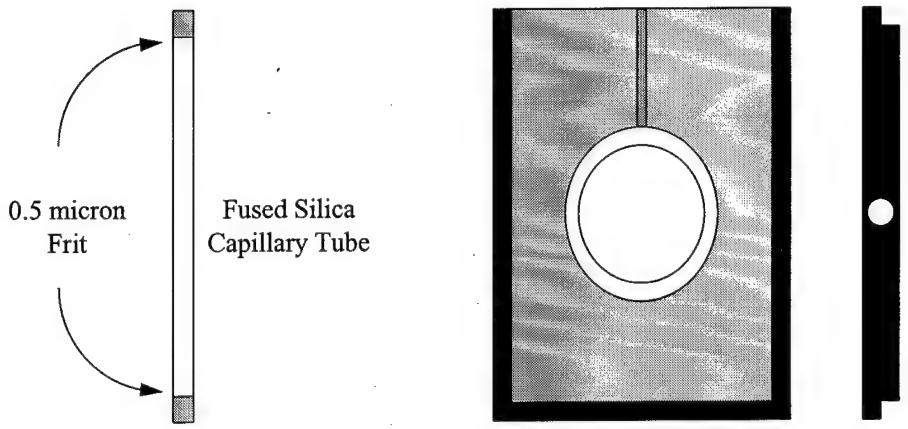

Figure 14: Raman Cell and IR Raman Cell Holder

The Raman cell is similar to the luminescence cell. For usage in a vis-Raman setup using the FL3-11 system, figure 13 shows the cell and holder, however, if the sample is to be placed in the Bomem MB Series with the Infrared Raman Attachment, figure 14 shows the cell with the required holder.

In order to fill the capillary cells with the powders, a Teflon funnel was fashioned. A cutaway sketch of the Teflon funnel is shown in figure 15. The open end of the capillary is pushed up from the bottom until it rests against the underside of the lip on the funnel. The capillary tube will be extending

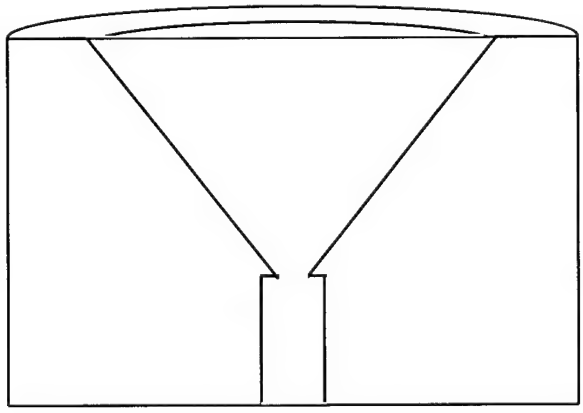

Figure 15:: Teflon Funnel for Filling Capillaries with Fine Powders

beyond the bottom of the filler. The powdered sample is then placed into the top portion of the funnel and scraped into the capillary tube with a 28 gauge wire. Once the capillary is filled to the desired level, the material is removed from the funnel, and the capillary extracted. A 0.5 micron frit is then epoxied to the open end of the capillary. The cell is now ready for use.

A materials list for the apparatus and the cells is located in Appendix A.

B. Standards

Samples of labeled UO_2, U_3O_8, and UO_3 were obtained as standards for this study. These standards are to be qualitative standards. The UO_2 used for standards is pulled from the same source as the samples used for weathering. External standards include the use of CeO_2, De-I water, and Diamond Dust. Internal standards of diamond dust were utilized for the DRIFTS samples as well as the fluorescence and Raman samples. In a paper by Cardona [CAR/94] it is stated that diamond is Raman active with a peak at approximately 1320 cm^{-1}. Several standards are utilized to ensure that the spectrometers are working properly and that they are being utilized properly.

1. Fluorescence Standards

Two standards were utilized for the FL3-11 system. Ovalene and europium chloride were utilized as the fluorescence standards. The ovalene was chosen because it has its greatest fluorescence response

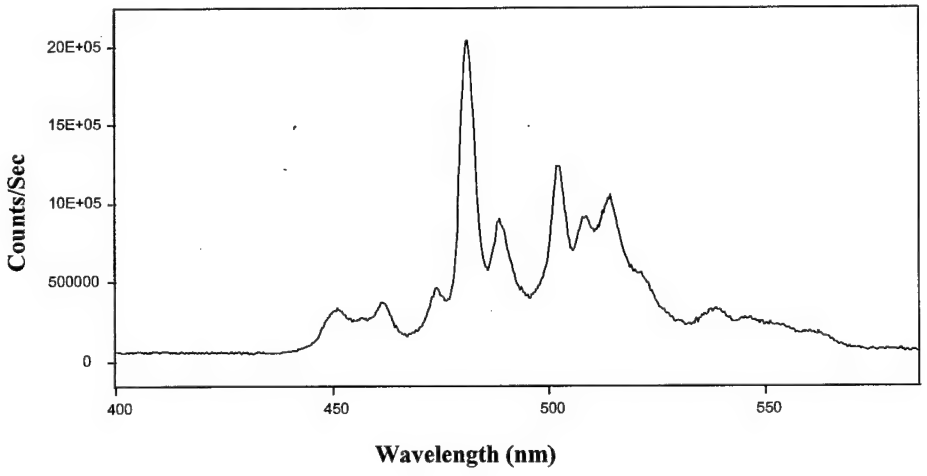

Figure 16: Ovalene Fluorescence Standard, 342 nm Excitation, 2.0 nm Excitation x 2.0 nm Emission Slits, Corrected Spectra

when excited at 342 nm, which was thought to be in the region used for excitation of the uranium oxides. Figure 16 shows the corrected luminescence spectra of the ovalene standard when excited at 342 nm with 2.0 nm excitation and 2.0 nm emission slits. The peak at 481 nm is located where it should be, according to the literature. Also, that peak maintains the proper relative intensity as compared to the triplet peak between 505 and 520 nm as stated in the literature.

Europium chloride was chosen because it is a lanthanide that is believed to give both atomic and molecular fluorescence spectra consisting of sharp, well-defined peaks. Figure 17 shows the corrected luminescence spectrum for the europium(III) chloride when excited at 393 nm with 2.0 nm excitation and 2.0 nm emission slits. It is easy to see the sharp, well-defined peaks which led to the choice of this compound.

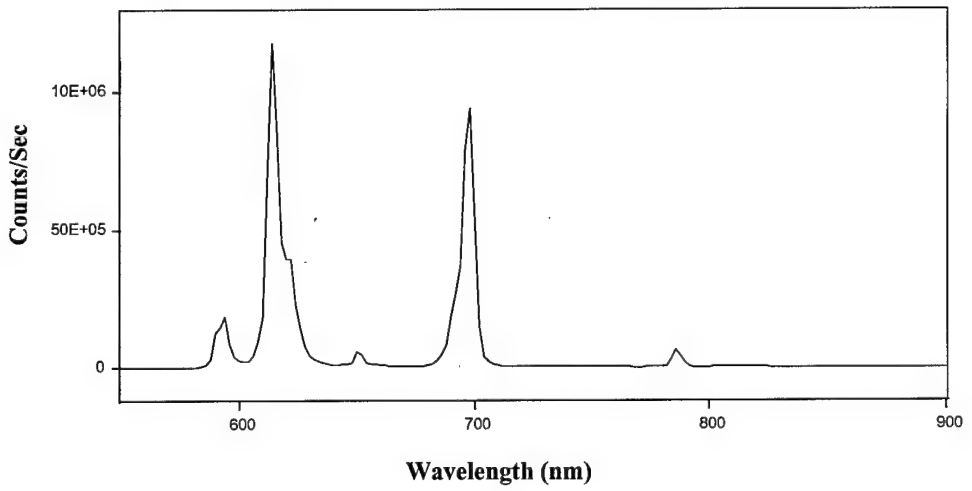

Figure 17: EuCl3 Fluorescence Standard, 393 nm Excitation, 2.0 nm Excitation x 2.0 nm Emission Slits, Corrected Spectra

The $EuCl_3$ luminescence spectra obtained here is consistent with the literature in peak location and relative peak intensities. The ovalene standard was also consistent with the literature. These two standards give reproducible spectra and are used often as standards in the field of fluorescence spectroscopy.

2. Infrared Standards

Diamond Dust is used as the background material for the DRIFTS analysis. The plots are presented in Kubelka-Munk units, standard notation for DRIFTS analysis, except where noted. Kubelka-Munk units are related to the reflection spectra, and sample concentration, by the relation

$$f(R_\infty) = \frac{(1 - R_\infty)^2}{2R_\infty} = \frac{2.303\varepsilon\ c}{s} \tag{11}$$

where

$f(R_\infty)$ = Kubelka-Munk units

R_∞ = Reflectance from an "infinitely thick" sample

ε = molar absorptivity

c = molar concentration of sample

s = scattering factor, dependent on particle size of sample

Figure 18 shows a background used for the DRIFTS measurements. The DRIFTS cell was filled with diamond dust and the KRS-5 window was epoxied to the cell, sealing it. The diamond dust used was

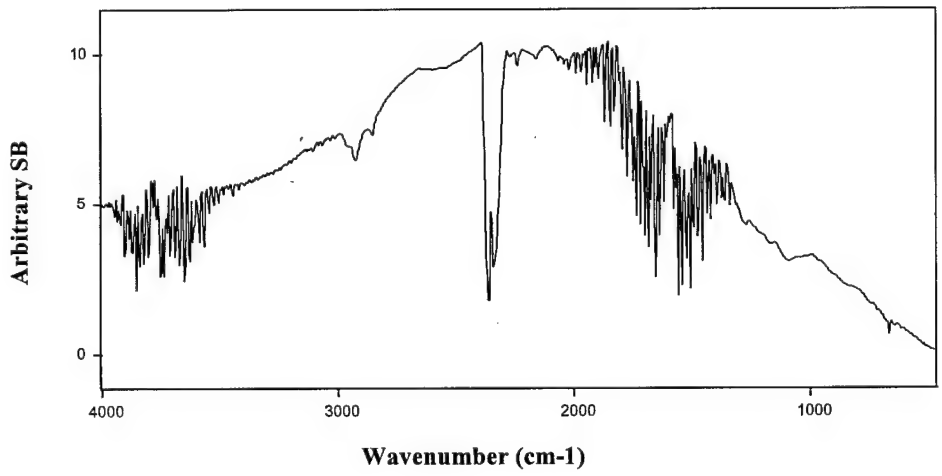

Figure 18: Background Spectra of Diamond Dust in DRIFTS Cell with KRS-5 Window and Epoxy

baked at 300° C for 3 hours to drive off any water that may have been trapped in the powder. The water lines present, 1400 - 2000 cm^{-1} and 3500 - 3900 cm^{-1}, as well as the CO_2 lines at 2250 and 2300 cm^{-1}, are believed to be from the air in the pathlength of the Bomem spectrometer with the Graseby Selector.

3. Raman Standards

Diamond dust and CeO_2 are used as standards for the NIR Raman. Both compounds exhibit a single, strong Raman shift that is easily identifiable. Figure 19 shows the Raman spectra of the mixture of

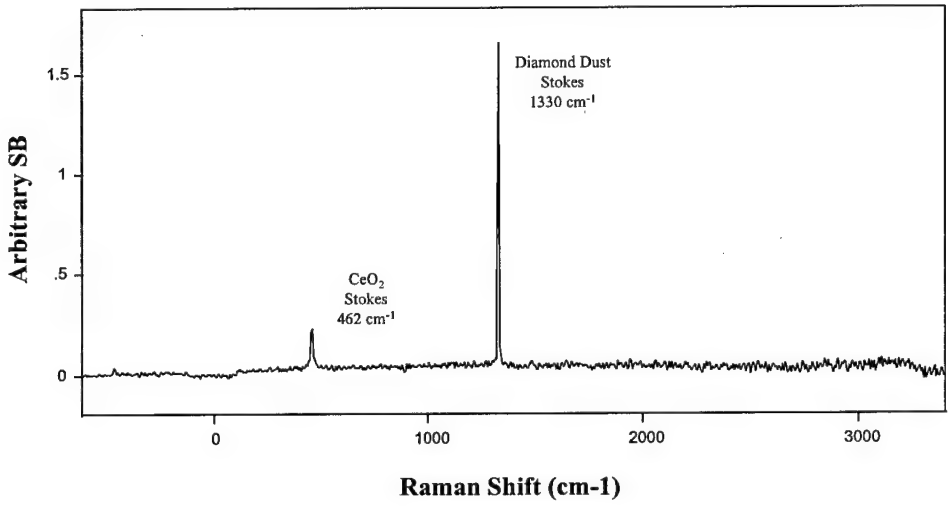

Figure 19: Diamond Dust:CeO_2 (11.3:1) NIR-Raman Standard

diamond dust and CeO_2 at a ratio of 11.3:1. The diamond dust Stokes shift is observed at 1330 cm^{-1} and the CeO_2 Stokes shift is observed at 462 cm^{-1}. With a good imagination, the anti-Stokes shift of the CeO_2 can be seen at -462 cm^{-1}, however, it is not labeled in this plot.

Pure CeO_2 is utilized as well. The Stokes shift of the pure CeO_2 is observed at 464 cm^{-1}. The anti-Stokes shift is observed at -464 cm^{-1}. Both of these shifts are shown in figure 20. The difference between the CeO_2 peaks in the diamond dust:CeO_2 mixture and the pure CeO_2 sample is less than the resolution, 4 cm^{-1}, of the system.

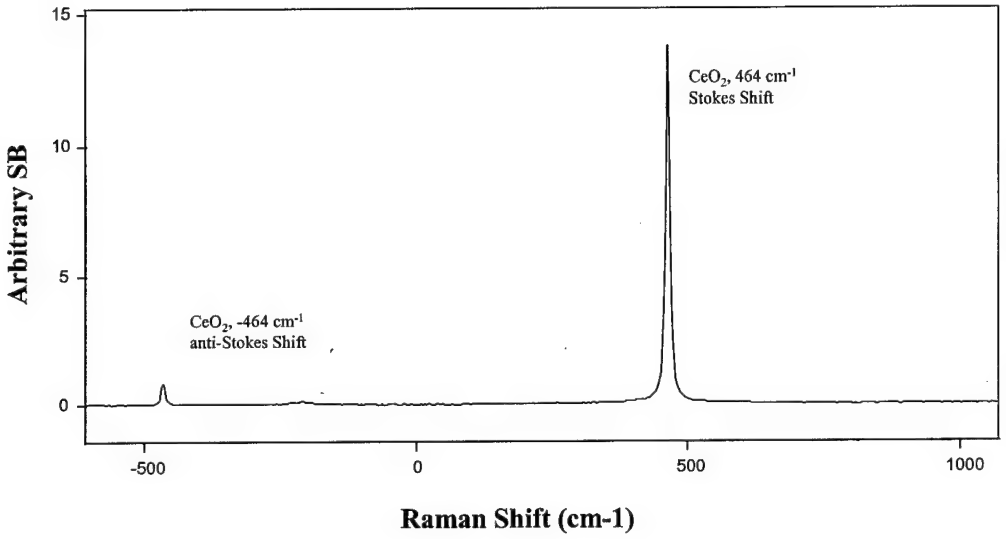

Figure 20: NIR-Raman Pure CeO_2 Standard

In the vis-Raman, set up with the FL3-11 and a 488 nm argon-ion laser, diamond dust is one of

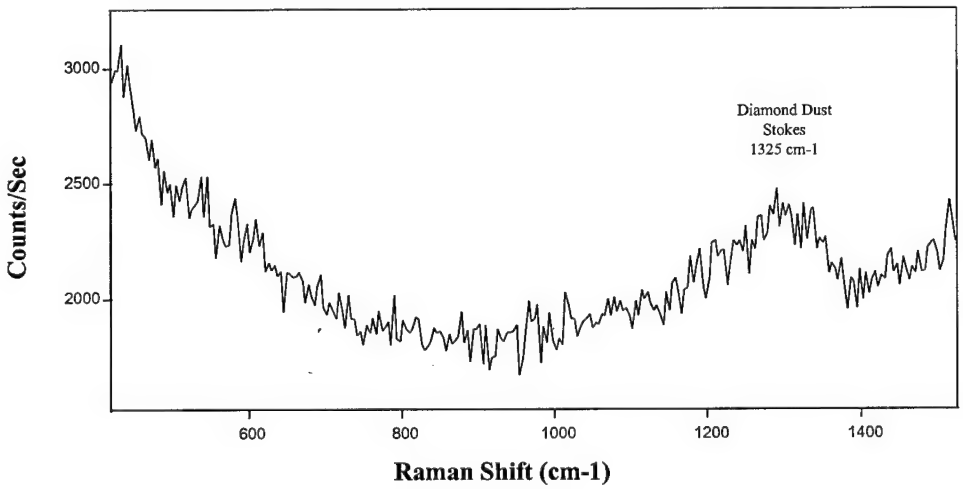

Figure 21: Vis-Raman Diamond Dust Standard

the standards utilized. The diamond dust Stokes shift is observed at 1325 cm^{-1}. The peak is not as sharp and well defined in the visible Raman as it is in the Fourier transform Raman. The reason for this is that FT-Raman has the capability of averaging over multiple scans, whereas this vis-Raman configuration can give only a single scan. Figure 21 shows the Stokes shift in the vis-Raman configuration using a 488 nm argon-ion laser as the excitation source.

Also used as a standard in the vis-Raman configuration is CCl_4. It is used because it has a strong Raman spectra and is easily identified. Figure 22 shows the Stokes shifts at roughly 315 and 458 cm^{-1}, with a possible peak at 715 cm^{-1}. The repeatability of this spectra is very good as the peak locations and intensities did not vary outside of the resolution of the system, 10 cm^{-1} with 1200 groove/mm gratings.

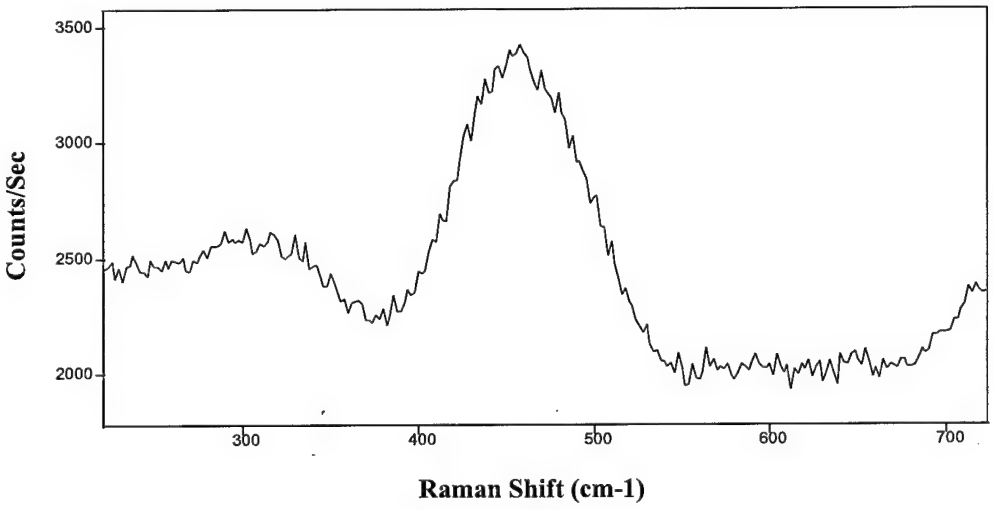

Figure 22: Vis-Raman CCl_4 Standard

C. Procedure

The procedure to obtain data from the weathered cells is very straightforward. At the desired intervals, 1 week, remove the cell from the weathering apparatus and place into the system which obtains the desired spectra. Compare this spectra to the previous spectra of the same sample. Note changes in the chosen peaks of interest to determine if the level of oxidation has changed.

In order to remove the cells from the weathering apparatus, the gas flow must be stopped. After the gas flow has stopped, the cells can be removed from the apparatus and placed into the cell holders for the individual techniques. This transfer must occur inside of the fume hood in which the apparatus is operating. A respirator, gloves, and full goggles must be worn during all transfers to lessen the risk of inhalation and personal contamination. Before the cells can be taken to the respective systems, a radiological survey of the fume hood and the cells must be accomplished to ensure that no loose contamination is present. The fluorescence system is located in a radioactive materials area, so no adverse precautions are required, save for those in place for such areas. The Bomem system used for the DRIFTS measurements is located in a radioactive materials area in building 640, however, the area is not cleared for radioactive materials storage. Due to this, any radioactive materials brought into this area cannot be left alone. Any time that the material is not in the immediate possession of an approved person, it must be under lock and key in an approved storage area. This requirement prevents the acquisition of spectra with very long integration times or very large numbers of scans.

The cells can only be transported from building 470 to building 640 and returned by a person listed as a permit user. This requirement is to eliminate accidental exposures to the base population by unaccountable personnel.

After the cells have been measured, a radiological survey must be completed of the used area before it can be cleared for general use. The action levels have been set at a level of six decays per minute of alpha radiation. Once the surveys have been completed and passed, the materials can be moved back to the weathering apparatus for insertion into the system. The cells are to be replaced into the apparatus and the gas flow restarted. The amount of time that each line is exposed to the outside environment is considered to be negligible as the air in each line is replaced every two hours. It is important to place the cells in the same location from which it was taken. This is to eliminate confounding factors in evaluation of the data.

IV. Results and Discussion

There were three major steps that needed to be accomplished before the measurement of any weathered samples were analyzed. The first step was construction and certification of the weathering apparatus, the second step was construction and certification of the cells to be used for weathering and analysis, and the third step was the analysis and benchmarking of standards.

A. Weathering Apparatus

The construction of the weathering apparatus, pictured in figure 10, was discussed in the previous chapter. The certification of the apparatus is a very important aspect of this thesis. The functionality of the weathering apparatus must be proven to work within the desired parameters to be certified. In certification of the weathering apparatus, gas flow rates, water drip rates, and temperature controls were tested. The requirements and results for each are listed in Table 13. The result values are averages taken over the duration of the test. The requirements were based on the desired lifetimes of the apparatus and its components.

Table 13: Certification Requirements and Results for Weathering Apparatus

Test	Requirement	Result	Time of Test
Gas Flow Rate (Line 1)	0.50 ± 0.10 liter/hour	0.60 liter/hour	12 hours
Gas Flow Rate (Line 2)	0.50 ± 0.10 liter/hour	0.55 liter/hour	12 hours
Gas Flow Rate (Line 3)	0.50 ± 0.10 liter/hour	0.57 liter/hour	12 hours
Gas Flow Rate (Line 4)	0.50 ± 0.10 liter/hour	0.53 liter/hour	12 hours
Gas Flow Rate (Line 5)	0.50 ± 0.10 liter/hour	0.48 liter/hour	12 hours
Gas Flow Rate (Line 6)	0.50 ± 0.10 liter/hour	0.57 liter/hour	12 hours
Water Drip Rate (Line 4)	6.06 ± 0.1 ml/hour	6.10 ml/hour	18 hours
Water Drip Rate (Line 5)	6.06 ± 0.1 ml/hour	6.02 ml/hour	18 hours
Water Drip Rate (Line 6)	6.06 ± 0.1 ml/hour	6.07 ml/hour	18 hours
Transformer/Heat Tape 1	40 ± 2°C	39.5°C	6 hours
Transformer/Heat Tape 2	140 ± 2°C	141.0°C	6 hours

The gas bottles were desired to sustain the system for longer than 260 days. If each bottle (2500 psi nominal) of gas supplies a dry and a wet line, with a flow rate of 1.0 liter/hour, the bottles were calculated to last 314 days.

$$\left(\frac{7.55 \times 10^{3}\, liters}{1.0\,\frac{liters}{hour}}\right) \times \left(\frac{1\ day}{24\ hours}\right) = 314.5\ days$$

With the error allowed in the flow rate, a maximum acceptable flow depletes the bottle in 262 days. Each line was tested independently of the other lines. The fact that the wet line supplied by each of the bottles has a different, and larger resistance to flow, head, than the dry line was not considered until after certification. When the apparatus was started with samples in the high temperature chamber, the differences in resistance to flow caused a lower flow rate in the wet lines and a higher flow rate in the dry lines. Thus, the gas supplies were depleted by one third in two days. At this point, the flow was stopped and a modification was made to the procedure. There would no longer be a constant flow of controlled gases over the sample cells, rather, each line would be purged individually on a daily basis. This maintains a static exposure environment and introduces exchanged gases while preserving gas supplies.

The drip rate into each pre-wetting chamber of the apparatus was controlled by a titration tube with a stopcock. The titration tubes were continually fed from a 20 liter reservoir of De-I water. Once an acceptable flow rate was established, it was monitored by measurement of the level of water dripped into a graduated cylinder, to ensure that the decrease of water in the reservoir did not affect the flow rate over a period of 18 hours. A four-line peristaltic pump has been obtained to replace the titration tubes, however it will not be placed into the apparatus until more gases can be obtained and a gas bottle changeover is performed. The relative humidity level of the gas leaving the pre-wetting chamber was chosen to be close, but below the salt solution maintained relative humidity in the wet lines of the apparatus. The salt solution used in the apparatus is a saturated NaCl solution in De-I water. This solution maintains a relative humidity of 76% at 25°C.

The humidity conditions and the temperature conditions were able to be maintained, however, the targeted flow rates of gases were not maintainable to the desired levels. Difficulties with the gas flow rates were due to the different resistance of flow between the wet and dry lines. The procedural change to a static exposure is acceptable as long as it is possible to exchange the gases around the sample periodically.

The two elevated temperature requirements were chosen to give a real world high temperature condition (40°C) and an accelerated weathering condition (140°C). The error allowed in the temperature controls is due to the combination of transformers, heat tape, and exposure chambers. The combination of the transformer and heat tape allows for control to approximately 0.5°C, however the chamber in which these temperatures are maintained is a large heat sink (stainless steel box), therefore, tolerances were given a factor of four margin. The temperatures were measured with a mercury thermometer placed in the center of the chamber. The temperatures recorded were taken six hours after the temperature had stabilized.

B. Weathering Cells

The use of uranium powders dictated the development of analysis cells that can contain the sample throughout the weathering process. For the fluorescence and the Raman cells, a fused silica capillary with 0.5 micron frits was utilized. The cell for the DRIFTS analysis was a little more complicated. The designs of these cells are discussed in Appendix A. Certification of these cells required that they meet three criteria. First they must contain the sample. Second, they must be usable for the technique desired. Third, weathering must occur in the cell without having to remove the sample.

In meeting the first criteria, containment of the sample, both designs performed well. By inspection, the fused silica capillaries with frits epoxied to the ends provided excellent containment of the sample. The DRIFTS cells, pictured in figure 11, has more openings to seal, however, with the KRS-5 and quartz windows epoxied in place, and the frits epoxied on the stainless steel capillaries, they provided excellent containment of the sample as well.

The second criteria dictated that any materials used in the cell designs would provide no interference in regions of interest for the desired techniques. The material for fluorescence cells must not fluoresce and must transmit in the UV portion of the spectrum. The Raman cells must not have Raman peaks that interfere with the sample signal. Finally, the DRIFTS cell had to have windows that could transmit in the infrared, out to roughly 25 microns, and transmit in the UV as well. The DRIFTS cell also had to limit specular reflections as much as possible. Fused silica capillaries, SPEX fluorescence free grade, were chosen as the cell material for the fluorescence cells because they do not fluoresce and they

transmit in the UV. Fused silica capillaries, SPEX fluorescence free grade, can also be used for the Raman cells since the SiO has only one Raman peak, located at 455 cm^{-1}, which is outside of the anticipated areas of interest for a Fourier transform Raman system. The DRIFTS cells were machined from stainless steel and have a KRS-5 window for the infrared transmittance requirement and a quartz window for the UV transmittance requirement. The cell is sloped to limit specular reflections.

To meet the third criteria, capability of exposure within the cell, an experiment to determine the diffusion rate of the frits was required.. Four cells were created to determine this value. The cells were prepared in a nitrogen environment at ambient pressure. They were then exposed to ambient conditions and allowed for diffusion of air through the frits. The cells were sealed at times of one week, three weeks and seven weeks, with one cell being the control. The intent was to measure the concentration of carbon monoxide in the cells to determine the diffusion rate. Carbon monoxide was chosen over carbon dioxide because a larger cell could be utilized. Since each cell is maintained at standard pressure, the cell is opaque at the CO_2 absorption lines due to the extremely high absorption cross section of CO_2. Our cell length of 19.5 cm yields a maximum CO_2 partial pressure of 0.039 Torr. Since we are working at ambient pressure, and our reference cell has the average atmospheric CO_2 partial pressure, 0.228 Torr, we are opaque in this region. Our maximum cell length for atmospheric partial pressure is 0.52 millimeters. The partial pressure of carbon monoxide at atmospheric pressure is 1.52E-4 Torr. The cell length is limited by the spectrometer to 21.0 cm. At a length of 19,5 cm, we are not opaque in the CO absorption bands. These measurements were never completed due to the Bomem DA Series Infrared Spectrometer required to make these measurements awaiting repairs.

C. Benchmarking of Weathering Standards

It was necessary to benchmark our starting point for the weathering in each technique. We know that we do not have a stoichiometric UO_2 as our starting point, however, we must be able to document the changes as the weathering continues. By benchmarking our starting point, we see what happens to our sample as the weathering process occurs. Table 5 gives a list of the figures for the benchmarked spectra used to compare samples against. It also shows the dilution ratios of the diamond dust mixtures used here.

Table 14: Benchmark Spectra Table

Figure	Technique	Sample	Diluted in Diamond Dust (DD:sample)	System	Slit Width (Ex/Em) or Gain Value
Fig. 16	Fluorescence	UO_2	9.64:1	FL3-11	4/2
Fig. 17	DRIFTS	UO_2	9.64:1	Bomem	E (gain)
Fig. 18	Fluorescence	U_3O_8	9.20:1	FL3-11	4/2
Fig. 19	DRIFTS	U_3O_8	9.20:1	Bomem	E (gain)
Fig. 20	Fluorescence	UO_3	10.50:1	FL3-11	4/2
Fig. 21	DRIFTS	UO_3	10.50:1	Bomem	E(gain)
Fig. 22	DRIFTS	U oxides	each as above	Bomem	as above
Fig. 23	Fluorescence	CeO_2	11.30:1	FL3-11	4/2
Fig. 24	DRIFTS	CeO_2	11.30:1	Bomem	E (gain)

The following two plots are the benchmark of the UO_2 sample that is being weathered. Figure 23 shows the luminescence of the UO_2 standard as compared to background. This spectra was obtained with the ISA/SPEX Fluorolog 3, FL3-11 system. The excitation slit settings were 4.0 nm and the emission slit

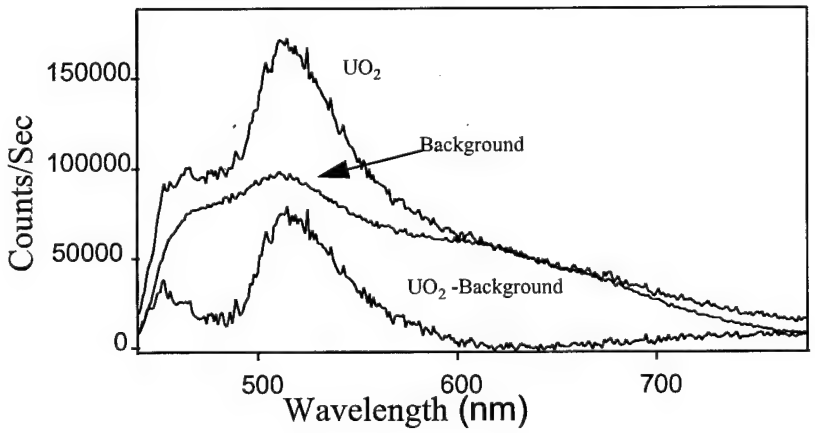

Figure 23: Fluorescence Benchmark of UO_2, Background, and Background Subtracted Spectra

settings were 2.0 nm. The excitation wavelength was 425 nm. Peaks can be seen at 452 nm and 515 nm with shoulders located at 465, 488, 505, 529, 537, and 543 nm. There were two filters used, on the excitation side a 450 nm short pass with a Corning 3-72 long pass on the emission side. The background spectrum was obtained under the same settings and subtracted from the UO_2 spectra to obtain the background subtracted spectra.

Figure 24 is the DRIFTS benchmark. This plot shows a pure UO_2 sample versus a sample of UO_2

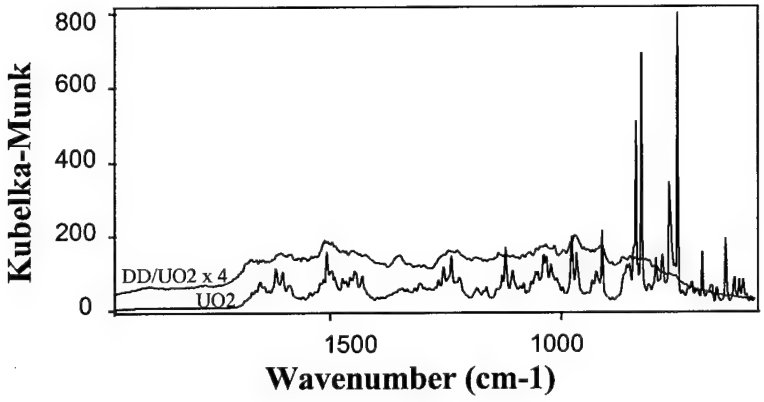

Figure 24: DRIFTS Benchmark DD/UO_2 and pure UO_2

diluted in diamond dust. This spectra was obtained from the Bomem MB with the Graseby Selector. The peaks of interest are 960, 856, and 754 cm^{-1}, based on literature values. The changes, relative intensity and relative peak area, in these peaks gives an indication of the amount of oxidation that has occurred. Other peaks that can be identified are the doublet peak between 1500 and 1700 cm^{-1}, water, the doublet peak at 2850 and 2920, C-H stretch (seen in appendix), the doublet peak between 3200 and 3800 cm^{-1}, water (seen in appendix), and a peak at 1350 cm^{-1}, diamond.

The following two plots are for the U_3O_8 that is used as a reference. Figure 25 shows the luminescence of the U_3O_8 as obtained from the ISA/SPEX Fluorolog 3, FL3-11 system. The excitation slit settings were 4.0 nm and the emission slit settings were 2.0 nm. The excitation wavelength was 425 nm.

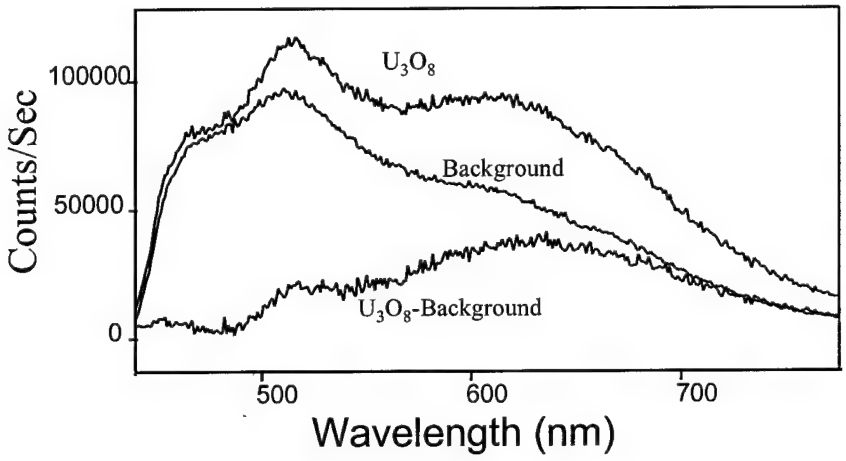

Figure 25: U_3O_8 Benchmark Reference Spectra, Background, and Background Subtracted U_3O_8

Peaks can be seen at 453 and 518 nm with a very broad peak centered on 635 nm. There were two filters used, on the excitation side a 450 nm short pass with a Corning 3-72 long pass on the emission side. The background spectrum was obtained under the same settings and subtracted from the U_3O_8 spectra to obtain the background subtracted spectra.

Figure 26 is the DRIFTS reference spectrum for the U_3O_8 standard. This plot shows a pure U_3O_8 sample versus a sample of U_3O_8 diluted in diamond dust. This spectra was obtained from the Bomem MB

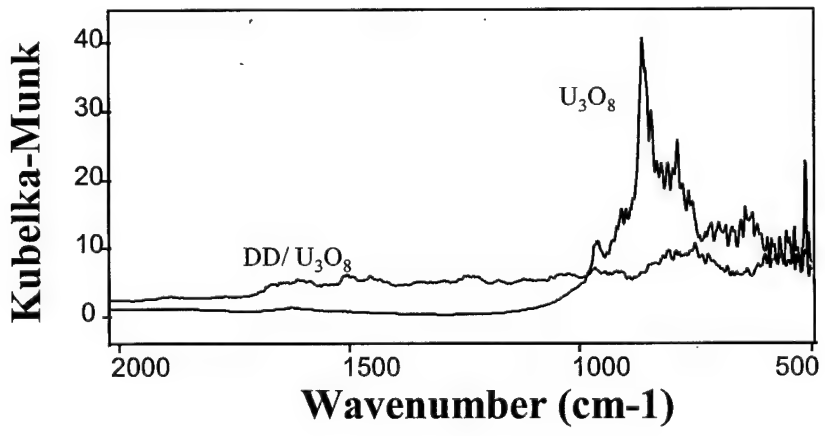

Figure 26: DRIFTS Reference DD/U_3O_8 and Pure U_3O_8

with the Graseby Selector. The peaks of interest are 960, 856, and 754 cm^{-1}. Again, other peaks that can be identified are the doublet peak between 1500 and 1700 cm^{-1}, water, the doublet peak at 2850 and 2920, C-H stretch (seen in appendix), and the doublet peak between 3200 and 3800 cm^{-1}, water (seen in appendix).

The following two plots are for the UO_3 that is used as a reference. Figure 27 shows the luminescence of the UO_3 as obtained from the ISA/SPEX Fluorolog 3, FL3-11 system. The excitation slit settings were 4.0 nm and the emission slit settings were 2.0 nm. The excitation wavelength was 425 nm. Peaks can be seen at 509 and 529 nm with shoulders at 492 and 553 nm. There were two filters used, on the excitation side a 450 nm short pass with a Corning 3-72 long pass on the emission side. The background spectrum was obtained under the same settings and subtracted from the UO_3 spectra to obtain the background subtracted spectra.

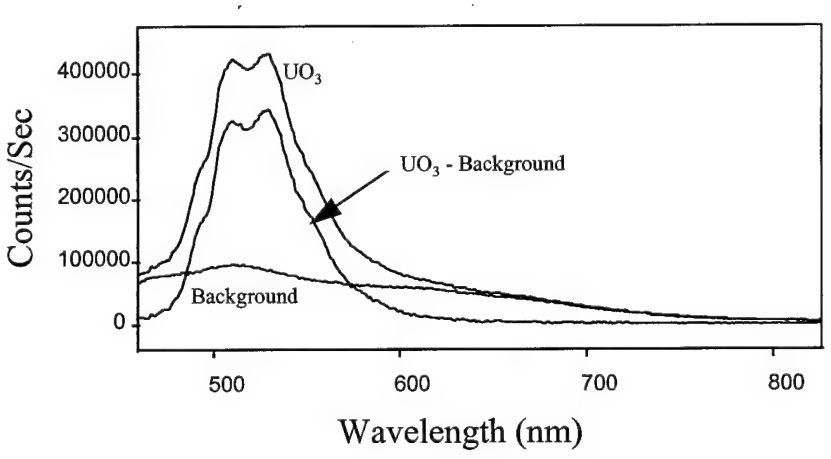

Figure 27: Fluorescence UO_3 Benchmark, Background and Background Subtracted Spectra

Figure 28 is the DRIFTS reference spectrum for the UO_3 standard. This plot shows a pure UO_3 sample versus a sample of UO_3 diluted in diamond dust. This spectra was obtained from the Bomem MB

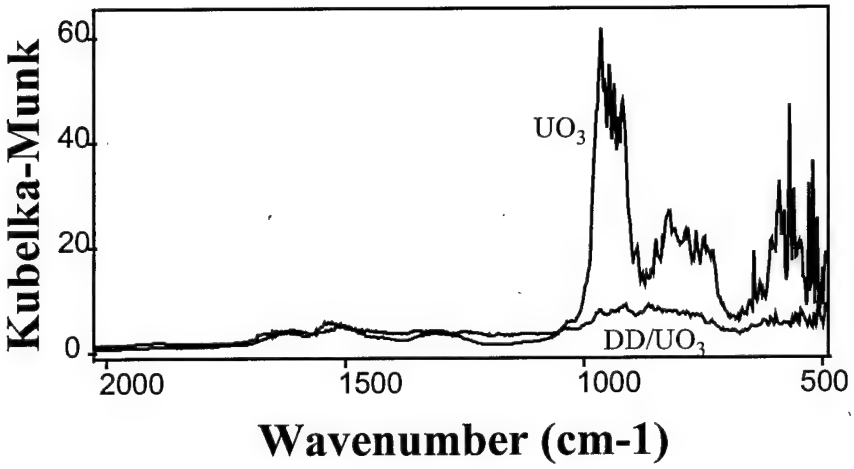

Figure 28: DRIFTS Reference DD/UO_3 and Pure UO_3

with the Graseby Selector. The peaks of interest are 960, 856, and 754 cm^{-1}. Again, other peaks that can be identified are the doublet peak between 1500 and 1700 cm^{-1}, water, the doublet peak at 2850 and 2920, C-H stretch (seen in appendix), and the doublet peak between 3200 and 3800 cm^{-1}, water (seen in appendix).

To be an effective measure of oxidation, there must be a measurable difference in the spectra as the oxidation occurs. Figure 29 shows the infrared spectra, in absorbance units, of the three uranium oxides on the same plot with the peaks of interest identified. As can be seen in this figure, a definite difference between the three oxides exists in the infrared.

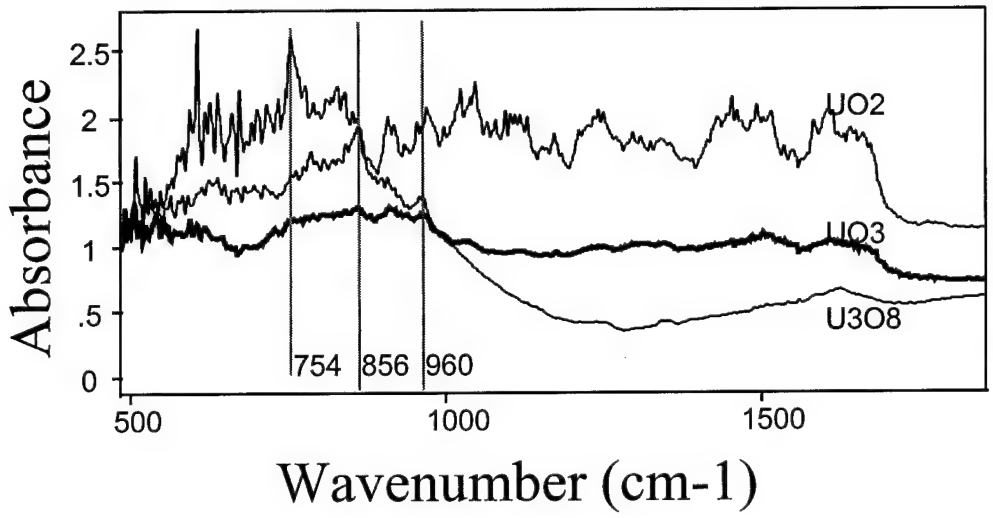

Figure 29: Infrared Absorbance Spectra of UO_2, U_3O_8, UO_3, with Peaks of Interest Marked

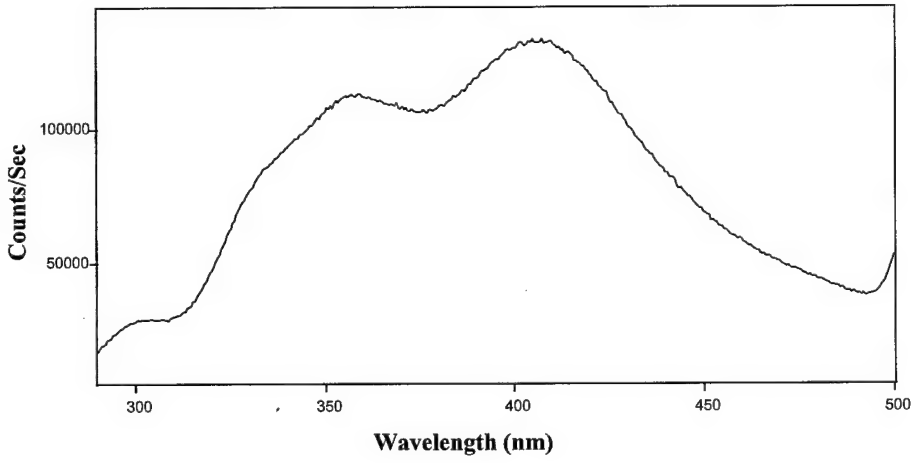

Figure 30: Fluorescence Benchmark of CeO_2, 272 nm Excitation, 2.0 nm x 2.0 nm Slits

Cerium dioxide is also benchmarked for surface deposition concerns in the weathering apparatus. The fluorescence spectra is shown in figure 30. The excitation wavelength is 272 nm with 2.0 nm excitation and 2.0 nm emission slits. Broad peaks are seen at 302, 361, and 415 nm with a week shoulder visible at 330 nm.

The DRIFTS spectra of the cerium dioxide in shown in figure 31. There are peaks at 1060 and 700 cm^{-1} which correspond to a shift from the absorbance spectra in the literature, but are consistent. A peak that is in the literature that is not present is a peak at 800 cm^{-1}.

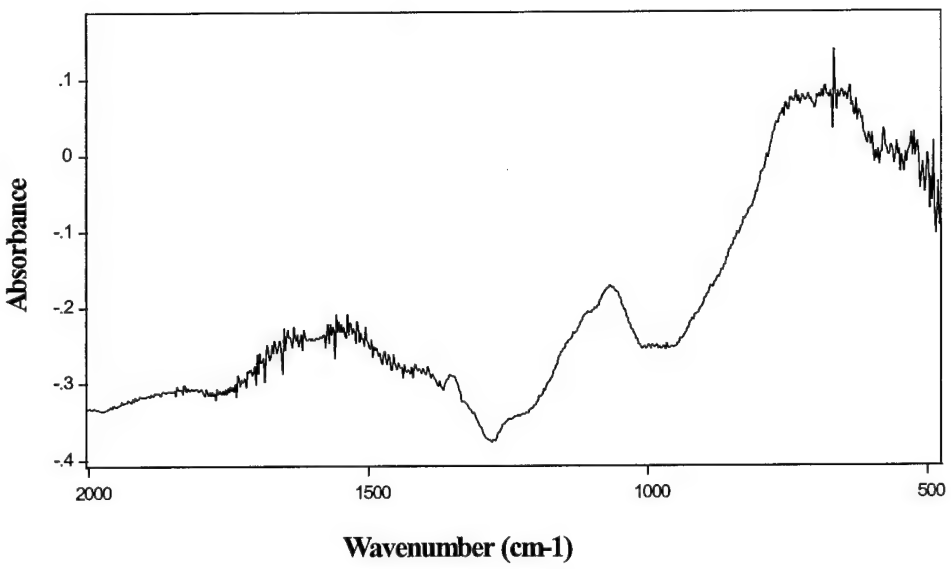

Figure 31: DRIFTS Benchmark of CeO_2

The spectra shown above were the result of measurements taken with the equipment listed in Table 2. Tables 15 - 19 show how the peaks in the benchmarked spectra compare to the literature. It is observed that no literature values could be found for the U_3O_8 luminescence spectra. It is believed that this is the first tabulation of these values. Only two sources of the luminescence of UO_2 were discovered. The luminescence of UO_3 was found mostly as the luminescence of the UO_2^{2+} ion, but there were several sources for UO_3, as well. The infrared spectra of the uranium oxides were quite prevalent as all three oxides dealt with here are represented well in the literature.

Table 15: DRIFTS UO_2 Literature Comparison

Peaks Observed Here (cm^{-1})	[POW/84]	[FUL/83]	[ALL/94]	[YU/88]
			330	
			345	
			430	
				440
			450	
			510	
530				530
	575			
			700	
820				
1375		1375		
1500		1500		

Table 15 shows a comparison between the infrared absorption peaks found in the literature and the peaks observed here. The peaks similar to those seen in literature are at 530, 1375, and 1500 cm^{-1}. A peak was observed here at 820 cm^{-1} that does not correspond to the literature as presented above. Of more interest here is the lack of peaks at 960, 856, and 754 cm^{-1}, which are prominent peaks in the UO_3 to be used for identification of the +6 oxidation state of the uranium.

Table 16: Luminescence UO_2 Literature Comparison

Peaks Observed Here (nm)	[WIN/84]	[WIN/86]
452		
465(sh)		
	470	470
488 (sh)		
505		
515		
537		
543		

Table 16 shows the comparison between the UO_2 luminescence observed here and the values found in the literature. The shoulder seen at 465 nm can be argued to be consistent with the peak at 470 nm seen in the literature. The other peaks seen here are indicative of a UO_2^{2+} presence in the sample. It was known that the sample of UO_2 utilized for this study was not stoichiometric and we therefore expected to see some U^{+6} in the sample.

Table 17: DRIFTS U_3O_8 Literature Comparison

Peaks Observed Here (cm^{-1})	[EID/85]	[ALL/94]	[YU/88]
		445	465
		510	548
725			
754			
	735	740	737
856			
910			911
960			

Table 17 shows a comparison between the peaks seen here for the DRIFTS U_3O_8. The peak seen at 910 cm^{-1} is comparable with the peak reported by [YU/88] at 911 cm^{-1}. Again, the other peaks observed here are indicative of the presence of UO_2^{2+} in the sample. The peaks listed at 445 and 548 were not observed here. The limit of the detector used is 450 cm^{-1} and noise was observed to overwhelm the signal at less than 525 cm^{-1}.

Table 18: DRIFTS UO_3 Literature Comparison

Peaks Observed Here (cm^{-1})	[FOD/65]	[ALL/94]	[YU/88]
		380	
		437	467
560			558
600			
754		726	723
	800	802	790
856		868	874
960	925		932

Table 18 shows the DRIFTS UO_3 peak comparison to literature. The peaks in the literature at 380 and 467 cm^{-1} were not observed due to detector limitations. The other peaks observed are comparable to the peaks found in the literature. The peak at 560 cm^{-1} agrees very well as the peaks at higher wavenumbers show a slight shift in position that is not altogether consistent.

Table 19: Luminescence UO_3 Literature Comparison

Peaks Observed Here (nm)	[BRI/80]	[PER/84]
492	488 (491)	
509	510	507
529	533	533
553	558	555

Table 19 shows the luminescence UO_3 peak comparison to the literature. As can be seen in the table, the peaks observed here agree very well with the published literature. There is little discrepancy between peak locations. There are only two comparisons to literature values made in the UO_3 because of the lack of UO_3 references in the literature. There are several spectra of UO_2^{2+} with most. The choices appear to have the greatest similarity to our sample types.

D. Lessons Learned

There were several things that were attempted in this thesis that led to undesirable results. This section attempts to explain those attempts to dissuade their repetition in the future. These are presented not as failures, rather as learning experiences for the researchers involved.

1. DRIFTS Attachment and Cell Design

The original intention was to use the Spectratech Baseline diffuse reflectance adapter for the Bomem MB series spectrometer. An infrared cell was designed to fit inside a slightly modified micro-sample cup that is a standard piece of equipment. The reason for this was due to its price, and its proven success on powdered samples in the past. The Spectratech Baseline posed difficulties that were unexpected at first, but then confirmed by Spectratech themselves. The Baseline was not designed for use with samples with a permanent window attached. Also, there were concerns about the dimensions of the window that would pass the infrared radiation to the sample. The initial design called for a window with a 3.0 mm diameter. This was determined to be inadequate because not enough radiation would reach the sample to provide a suitable signal. At this point, diffuse reflectance adapters from several manufacturers were evaluated. It was determined that the Harrick Praying Mantis and the Graseby Selector were the best choices. Both systems offered acceptable performance for our purposes. The Graseby Selector was chosen due to price considerations and has performed well. The cell designed for the Spectratech Baseline was not suitable for use with the Graseby Selector, therefore, a new cell was designed.

The original cell design was cylindrical in shape with air holes drilled on the sides for frits, and windows on the top and bottom. The cell had an outside diameter of 3.0 mm and an inside diameter of 2.5 mm, and a height of 6.0 mm. An infrared window could be attached to the top of the cell, and either a

quartz window, or a plug could be attached to the bottom. The infrared window would allow for transmission so that infrared spectra of the sample could be obtained, and the quartz window allowed for the exposure of the sample to UV radiation. The cells were machined from stainless steel. The major problem with this design is the size of the window for the incident infrared radiation to enter the cell. An aperture of only 3.0 mm diameter does not allow much radiation into the cell. With this small of an aperture, the spectra was expected to be very weak and concerns were raised as to the cell's suitability for the task.

The cell is pictured in figure 32. It shows a KRS-5 window as the infrared window, and the frits

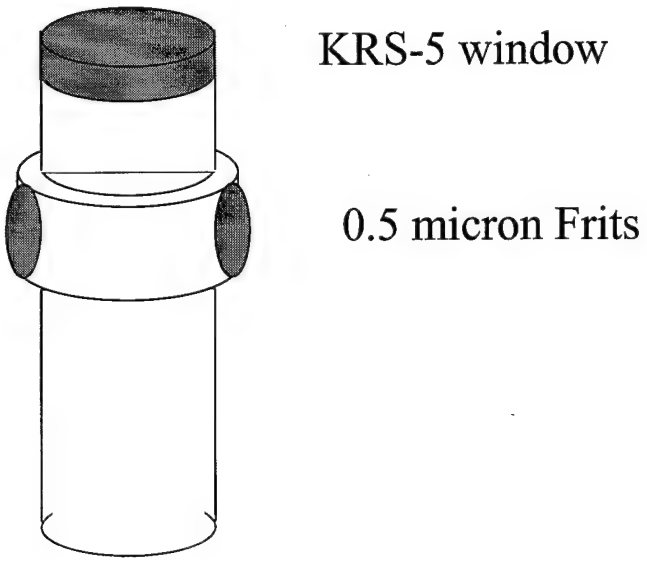

Figure 32: Original DRIFTS Cell Design

are shown in place. Ten of these cells were made, without windows, as backup cells in case the Graseby Selector did not arrive in time for this work. These cells were never filled with sample, or completely built (windows and frits attached).

2. NIR-Raman Spectroscopy

When working with solutions, NIR-Raman is a very suitable technique. However, when working with particles, the suitability of NIR-Raman can come into question. For our purposes, the primary

concern is heating of the sample due to the infrared laser (1.064 μm). The laser will heat the sample if the laser power is too high. For light colored oxides, such as CeO_2, the laser power could be taken to 0.5 Watt before a heating band would make itself apparent in the spectra. The bulk of our analysis is with black oxides. Black oxides, UO_2 is one, tend to absorb heat at a much better than light oxides. For this reason, the question of the usage of the NIR-Raman system for the UO_2 measurements arose. We contacted Edgar Etz at NIST, an expert in the field of Raman spectroscopy, to pose this question. His response was of cautious optimism, however, he would not recommend that it be attempted with our system. He offered to make the attempt at NIST and inform us of the results. His results[ETZ/97] determined that to obtain a usable Raman spectra, our system could not provide the required conditions of a long integration time and very low laser power (on order of 10 to 100 microwatts). Our laser is capable of controlled power output to only 50 milliwatts.

We conducted an experiment of our own to see the effects of a black oxide being placed in the system for analysis. We chose CuO as our black oxide. The melting point of the CuO is higher than any of the black uranium oxides. The particles were much larger than the particles of UO_2, so if any physical changes were observable under an SEM, we could assume similar physical changes could take place in the uranium oxides. Figure 33 shows an SEM image of a representative CuO particle prior to any exposure to the laser. Figure 34 shows an SEM image of a CuO particle after exposure to 0.20 Watts laser power for 60 seconds. It can be seen that the image in figure 32 has sharp, craggy features, whereas the image in figure 33 shows a smoothed, filled surface. It is believed that the CuO underwent a phase change while in the Raman system. Had this been uranium, the possibility of vaporizing a radioactive source could be argued to be very likely. Had this occurred, contamination of the Raman system

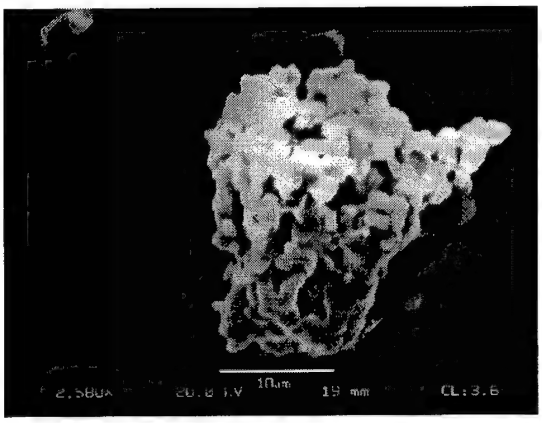

Figure 33: CuO SEM Image Before NIR Laser Exposure at 0.20 Watts

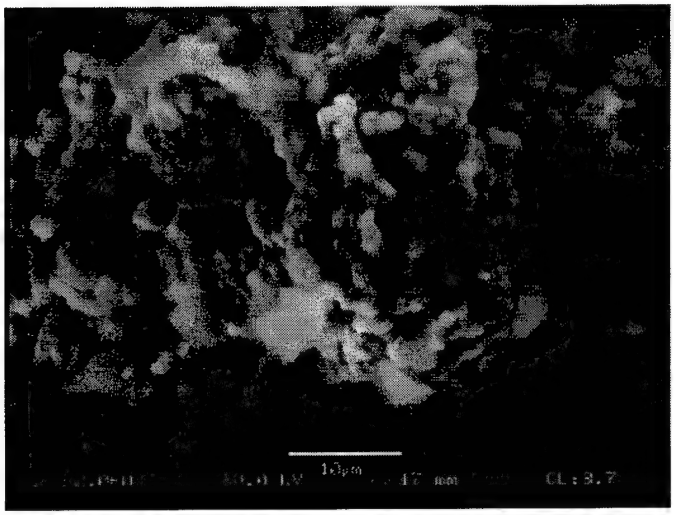

Figure 34: CuO SEM Image After Exposure to NIR Laser at 0.20 Watts for 60 seconds

Due to the advice given by Edgar Etz, and the CuO test accomplished here, the determination was made to not attempt acquisition of Raman spectra of any of the uranium oxides with the NIR-system. It was recommended that a visible Raman system be obtained for this purpose. The components for a visible Raman system are either on order, or in place at this time. This system, however, will not be a Fourier transform system, but a monochrometer system.

3. Weathering Apparatus

There are a few problems with the weathering apparatus as it is now built. The flow control from the gas supplies is inadequate. If a single gas bottle is to supply both a wet and dry line simultaneously, a valve is required on the dry line to enable matching of the flow resistance present in the wet line. Currently the resistance to flow is much greater in the wet line. When the flow is optimized for the wet line, it flows through the dry line at approximately 20 times the desired rate, as seen on the bubble flow meters. This causes the gas supply to be depleted much faster than desired. Had the apparatus been tested and certified with all lines operating, rather than testing each line individually, this problem would have been caught before the gas supply had been almost depleted.

Another area for improvement is the titration tubes used for drip-rate control in the pre-wetting chambers of the wet lines. At the present time, the drip-rates are controllable assuming a constant temperature, the drip-rate is set one time, and the temperature is assumed constant. If the temperature changes, the drip-rates must change to maintain the desired 65% relative humidity pre-wetting. If the temperature changes, the titration tube assembly cannot be adjusted without major impact to the apparatus and its gas line constituents. It is desirable to replaces the titration tubes with a peristaltic pump that allows for much greater flow control. A peristaltic pump is a compression pump that provides feed by compressing the tubing that carries the solution and forcing it out in controllable amounts. This pump is very similar to the IV pumps used by hospitals to deliver medications intravenously. A four line pump has been acquired, but is awaiting a fresh gas supply for the desired change.

The temperature chambers of the weathering apparatus need to be insulated. This is necessary to limit the possibility of worker injury, burns from the high temperature chambers, and to provide a more stable temperature environment. Currently, the chambers are fourteen inch cubes made from stainless steel. The walls of the boxes are very hot to the touch in the high temperature chambers and could cause injury. Also, temperature variations are more likely without insulation because steel is such a good thermal conductor.

V. Recommendations

Presented here are suggested courses of action for continuation of work presented in this thesis. Discussed are continuations of what was begun, and also possible directions to explore.

A. Continuation

Most importantly is the acquisition of new gas supplies. Without new supplies of gas, the apparatus cannot be opened unless the samples are to be considered disposable. It is possible that the apparatus could be opened to retrieve samples that are currently weathering, and the samples preserved. For this to occur, the samples would have to be placed into sealed containers with an inert environment, nitrogen or argon gas. Then the apparatus could be taken off line and the modifications could be made to the system. After modification to the apparatus are completed, the lines could be purged with the new gas supply, the samples could be replaced into the apparatus, and the weathering could continue.

More sample must be obtained. The amount of UO_2 obtained from NIST totaled 1.7 grams. This lack of material is what initially drove us to consider diluting the sample. It would be advantageous to analyze the weathering of a neat sample, alongside a diluted sample, for comparison. Also, the UO_2 obtained here is known to be UO_{2+x}, with $x<1$. This is because the sample has been exposed to the atmosphere on several occasions after its creation and before arriving at this location. Oxidation has occurred to these particles, but to what extent is currently unknown. Therefore, samples of stoichiometric UO_2 are desired. This will allow analysis of the initial stages of the oxidation as well as the intermediate to final stages. Caution should be taken if stoichiometric UO_2 is obtained, because as small particles, the sizes we are dealing with, UO_2 is very pyrophoric when in contact with oxygen. It has been known to ignite.

B. Possible New Directions

Micro-Spectroscopy is a valid suggestion for future study. Raman and photoluminescence of individual particles would be a logical step from the bulk materials we are working with here. Techniques for micro-Raman and micro-luminescence are used prevalently in the literature on individual particles. The spectrometers used in this work are able to accept accessories for micro sampling. They each can

accept third party accessories as well. In conjunction with the individual particle weathering, destructive measurement techniques may also prove useful. Low temperature measurements of weathered samples may give a precise, static look at the process. Other techniques such as conductivity measurements are able to provide composition information, on a bulk scale.

Perhaps limiting the weathering analysis to solid phase uranium oxides does not describe the entire process. What about the aqueous solutions of the uranium oxides? There may be much information that is easily obtained by Raman spectroscopy that may be unavailable by looking solely at solid phase material.

These suggestions are meant to say that there are numerous other approaches that may be taken to this provide options for solving this problem. The approach utilized in this thesis is just one of many possible. By no means are we implying that our approach is the best. It is a starting point. From here, many permutations are possible.

VI. References

[ALL/87] Allen, G.C., Butler, Anh Tuan "Characterisation of Uranium Oxides by Micro-Raman Spectroscopy", Journal of Nuclear Materials, Vol. 144: 17-19, 1987.

[ALL/93] Allen, G.C., Holmes "Characterization of Binary Uranium Oxides by Infrared Spectroscopy", Applied Spectroscopy, Vol. 48, No. 4: 525-530, 1994.

[ARM/89] Armstrong, D.P., Jarabek, Fletcher "Micro-Raman Spectroscopy of Selected Solid $U_xO_yF_z$ Compounds", Applied Spectroscopy, Vol. 43, No. 3: 461-468, 1989.

[BAR/89] Bartlett, J.R., Cooney "On the Determination of Uranium-Oxygen Bond Lengths in Dioxouranium(VI) Compounds by Raman Spectroscopy", Journal of Molecular Structure, Vol. 193: 295-300, 1989.

[BAU/84] Thurn, R., Kiefer, in Laser Processing and Diagnostics, Bauerle, D. (ed.), Springer, Berlin, 1984

[BRI/80] Brittain, H.G., Perry "Luminescence Spectra of the Uranyl Ion in Two Geometrically Similar Coordination Environments. Uranyl Nitrate Hexahydrate and Di-μ-aquo-bis[dioxobis(nitrato)uranium(VI)] Diimidazole", Journal of Physical Chemistry, Vol. 84: 2630-2634, 1980.

[BRI/81] Brittain, H.G., Perry "Photophysical Studies of Uranyl Comlexes. 2. Evidence for Splitting of the Luminescent Excited State of the Uranyl Ion", Journal of Physical Chemistry, Vol. 85: 3073-3078, 1981.

[CAR/94] Cardona,M. "Isotopic Effects In The Raman Scattering Of Diamond And Germanium", International Conference on Raman Spectroscopy, Vol. 14: 19-22, 1994.

[COL/74] Colmenares, C. "Infrared Spectroscopic Studies of the Surface Bond of Carbon Dioxide in Uranium Oxides", The Journal of Physical Chemistry, Vol. 78, No. 21: 2117-2122, 1974.

[COL/84] Colmenares, C.A. "Oxidation Mechanisms and Catalytic Properties of the Actinides", Progress in Solid State Chemistry, Vol. 15, No. 4: 276-364, 1984.

[EID/85] Eidson, A. "Infrared Analysis of Refined Uranium Ore", Analytical Chemistry, Vol. 57: 2134-2138, 1985.

[EKS/80] Ekstrom, A., Hurst, Randall, Loeh "UV-Visible and Infrared Spectra of Volatile Uranyl Complexes in the Gas Phase", Journal of Physical Chemistry, Vol. 84: 2626-2630, 1980.

[ETZ/97] Etz, Edgar S. Personal Correspondance. National Institute of Standards and Technology. Maryland, 8 October 1997.

[FOD/65] Fodor, M. , Poko, Mink "Investigation of Hydrolysis Products from Uranium Trioxide and Uranyl Salts by Derivitography and Infrared Spectroscopy", Symposium on Analytical Chemistry, 1965.

[FUL/84] Fuller, E.L., Smyrl, Condon, Eager "Uranium Oxidation: Characterization of Oxides Formed by Reaction with Water by Infrared Sorption Analysis", Journal of Nuclear Materials, Vol. 120: 174-194, 1984.

[GRA/90] Graves, P.R. "Raman Microprobe Spectroscopy of Uranium Dioxide Single Crystals and Ion Implanted Polycrystals", Applied Spectroscopy, Vol. 44, No. 10: 1665-1667, 1990.

[GRI/91] Griffiths, T.R., Hubbard "Absorption Spectrum of Single-Crystal UO_2: Identification of and Effect of Temperature on the Peak Positions of Essentially All Optical Transitions in the Visible to Near Infrared Regions Using Derivative Spectroscopy", Journal of Nuclear Materials, Vol. 185: 243-259, 1991.

[KAR/82] Karyakin, A.V. Mel'yantseva, Anikina "Effect of the Elemental Composition and Crystal Structure of a Matrix on the Luminescent Properties of Uranium", Zhurnal Prikladnoi Spektroskopii, Vol. 36, No. 6: 935-941, 1982.

[KER/73] Keramidas, V.G., White "Raman Spectra of Oxides with the Fluorite Structure", The Journal of Chemical Physics, Vol. 59, No. 3: 1561-1562, 1973.

[LID/95] Lide, D.R.., Edit., CRC Handbook of Chemistry and Physics, 76th Edition, CRC Press, Inc., pp. **15**-23.

[NOR/96] Northrup, J. Ed. Handbook of Nuclear Weapons Effects: Calculational Tools Abstracted from DSWA's Effects Manual One (EM-1), DSWA, Washington, D.C.,1996, pp. 167.

[NYQ/97] Nyquist, R. A. and Kagel, R. O. The Handbook of Infrared and Raman Spectra of Inorganic Compounds ant Organic Salts, Volume 4., Academic Press, Inc., 1997. pp. 228-231 and 490-491

[ORE/96] Orel, Z.C., "Structural And Electrochemical Properties Of CeO_2 And Mixed CeO_2/SnO_2 Coatings", Solar Energy Materials and Solar Cells, Vol. 40: 205-219, 1996.

[PER/84] Perry, D.L., Tsao, Brittain "Photophysical Studies of Uranyl Complexes. 4. X-ray Photoelectron and Luminescence Studies of Hydrolyzed Uranyl Salts", Inorganic Chemistry, Vol. 23: 1232-1237, 1984.

[POW/94] Powell, G.L., Dobbins, Cristy, Cliff, Meyer, Lucania, Milosevic "The Study of the Oxidation of Uranium by External and Diffuse Reflectance FTIR Spectroscopy Using Remote-Sensing and Evacuable Cell Techniques", SPIE Vol. 2089: 214-215, 1994.

[RIT/81] Ritchie, A.G. "A Review of the Rates of Reaction of Uranium with Oxygen and Water Vapour at Temperatures up to 300°C", Journal of Nuclear Materials, Vol. 102: 170-182, 1981.

[RIT/83] Ritchie, A.G. "The Kinetics of the Uranium-Water Vapour Reaction - An Evaluation of Some Published Work", Journal of Nuclear Materials, Vol. 120: 143-153, 1983.

[RIT/85] Ritchie, A.G. "The Kinetics of the Uranium-Water Vapour Reaction Between 40°C and 100°C", Journal of Nuclear Materials, Vol. 139: 121-136, 1985.

[RIT/86] Ritchie, A.G., Greenwood, Randles, Netherton, and Whitehorn "Measurements of the Rate of the Uranium-Water Vapour Reaction", Journal of Nuclear Materials, Vol. 140: 197-201, 1986.

[SAM/73] Samsonov, G.V., Ed. The Oxide Handbook, Trans. from Russian by C. Nigel Turton and Tatiana I Turton, IFI/Plenum, Washington, 1973.

[SCH/87] Schoenes, J. "Recent Spectroscopic Studies of UO_2", Journal Chem. Soc., Faraday Trans. 2, Vol. 83: 1205-1213, 1987.

[SKO/92] Skoog, D. A., and Leary, J. J., Principles of Instrumental Analysis, Fourth Edition, Saunders College Publishing, pp 176, 1992.

[WEA/85] Weast, Robert. C. (ed.). CRC Handbook of Chemistry and Physics, 66th Edition, CRC Press, Inc., pp. **D**-91, **D**-127, 1985

[WIN/84] Winer, K., Colmenares, Wooten "Cathodoluminescence of Uranium Oxides", Journal of Luminescence, Vol. 31 & 32: 357-359, 1984.

[WIN/86] Winer, K., Wooten, Colmenares, Smith "Luminescence of Thin Uranium Oxide Films", Journal of Luminescence, Vol. 35: 311-319, 1986.

[YU/88] Yu, B., Hansen "The FTIR Study of Uranium Oxides by the Method of Light Pipe Reflection Spectroscopy", Mikrochim. Acta, I:189-194, 1988.

Appendix A: Materials

This appendix contains material lists and justifications for all of the designed equipment used in this thesis.

Table 20 is a materials list for the weathering apparatus design. The justification for each item over other possible options is discussed here.

Table 20: Materials List for Weathering Apparatus

Material	Quantity	Usage	As Seen In
Teflon Tubing	300 feet	Gas Flow Line	fig. 11
Glass Tubing (1 " diameter, threaded both ends)	3	Pre-Wetting Chamber	fig. 11
Side Arm Flask	3	Humidity Control Chamber	fig. 11
Threaded Glass Test Tubes (1 " diameter, w/ Teflon lined caps)	48	Cell Containers	fig. 11
Peristaltic Pump (4 line)	1	Pre-Wetting Drip Control	fig. 11
Bubble Flow Meter	6	Gas Flow Rate Control	fig. 11
Inline Filter (1 micron)	6	Gas Line Filter	fig. 11
HEPA Filter (0.25 micron)	6	Exhaust Filter Assembly	fig. 11
Glass Reservoir (20 L capacity)	1	De-I water Container	fig. 11
Stainless Steel Box (14" cube)	4	Exposure Chambers	fig. 11
Power Transformer	2	Heating Element Power Control	
Heat Tape (6 ft. length)	4	Heating Element	
Test Tube Rack/Support (capacity: 36)	4	Cell Container Supports	
HPLC Filter (1 micron)	3	Humidity Control Chamber Bubbler	
Teflon Stoppers	13	Glass to Tubing Connectors	
Brass Toggle Valves	6	Line Shut-off Valves	
Aluminum Brick (In-Line Filter Support, 4"x6")	1	Inline Filter Support Rack	
Master Bond Epoxy (Hi-Vacuum) {part no. EP21TDCHT}	1 pint	Sealing of Connections	
UV Lamp (short/long wave)	1	UV Exposure Chamber	

The gas flow lines used Teflon tubing. Other options were to use stainless steel tubing, poly tubing, or a latex tubing. Stainless steel tubing was removed from consideration because of its inflexibility. Once Stainless steel tubing is bent to shape, it is very difficult, if not impossible to alter the configuration without discarding the already bent piece. Poly tubing and latex tubing were removed from consideration because both materials allow gases to diffuse through them. It is desirable in this project to have a

completely known environment inside of the system. The choice of the dual threaded glass tubes for the pre-wetting chambers was mainly for diffusion concerns. Each of these pieces was made by the glass blower on Wright-Patterson AFB by opening the closed ends of two threaded test tubes and connecting them together. Pyrex carrier gas drying tubes were considered for use as the pre-wetting chambers because they were available on site, however, their small openings on each end, roughly three-eighths inch diameter, made working with them difficult. The carrier gas drying tubes required Teflon stoppers drilled to accept two one-fourth inch diameter Teflon tubing. The physical size of components drove the selection of the dual threaded glass tube. The caps of the tubes, one inch diameter, were drilled to accept two one-fourth inch diameter Teflon tubing.

The side-arm flasks were chosen for use as the humidity control chambers for the multiple arm capability. The humidity control chambers needed to have a way for the air to get into the salt solution and a way for the humidified air to get out of the chamber. In this case, dry air is coming in through the top opening of the flask, is bubbled through the salt solution, then exits through the side arm of the flask. The component that allows the gas flow to bubble through the salt solution is a 1.0μ HPLC frit. The frit is made of stainless steel and breaks the gas flow into very tiny bubbles, on the order of 10μ. This greatly increases the surface area of gas that comes in contact with the salt solution and ensures that the desired humidity will be reached.

In order to maintain a constant drip-rate in the pre-wetting chambers, a peristaltic pump was chosen. This pump is capable of maintaining flow rates of less than 1.0μL/min. The apparatus was not built with the peristaltic pump in place, however. It was built with titration tubes using gravity to control the drip-rate. This solution provides an accuracy much less than that desired. This solution can maintain the system so long as the water reservoir is constantly maintained at the same level. If the reservoir gets too low, less than 19.0 liters, in volume, then the drip-rate will slow to unacceptable values. The depletion of approximately one liter of water from the reservoir takes about two and a half days. This would suggest daily refilling of the reservoir. The peristaltic pump is not dependent upon gravity for its flow control.

Therefore, once started, the weathering apparatus with the peristaltic pump in place could operate for five to six weeks without having to refill the reservoir.

A bubble flow meter was placed at the end of each line in the weathering apparatus so that the actual flow rate of the line could be measured. Other types of flow meters were considered, however, their cost prohibited their use. Also, the possibility of radioactive contamination of the weathering apparatus components drove the choice to the least expensive products. The Inline filters were used to eliminate any particulate contaminants that may have been present in the gas supply. These filters used 10.0μ frits to filter the air. 1.0μ frits were obtained for possible insertion into the inline filters, however, it was decided that the 10.0μ frits were sufficient as the gases were certified particulate free. The HEPA filters were used to filter the gas at the end of each gas line before being exhausted into the fume hood. Their purpose was to prevent any possible loose contamination inside the weathering apparatus from escaping into the fume hoods. The HEPA filters used were rated at 0.25μ.

The glass reservoir was chosen over poly reservoirs and Nalgene reservoirs for the same reasons that Teflon tubing was chosen over poly and latex. Both poly and Nalgene allow gases to diffuse through them. This would have allowed for gases to dissolve into the water and possibly contaminate the weathering apparatus with unwanted gases in the lines. Glass was chosen over Teflon because of cost and availability. A glass reservoir was available on site, whereas a Teflon reservoir would have had to have been purchased. The stainless steel boxes used for the weathering chambers were chosen over aluminum because of ease of construction. The stainless steel sheet metal was on hand and could be bent to build a box with equipment available in the AFIT shop. Aluminum sheet metal was not readily available. Had the aluminum been available, it would have been a better choice of material because of its heat conduction properties. Either metal was desirable over wood because of the structural stability. Scorching and drying of the wood in the high temperature chambers would have been a major concern. Also, wood is very porous and could contain particles within the grain.

Threaded glass test tubes were chosen as the cell containers within the weathering chambers due to the need to have separate conditions in each chamber. The cells could not be placed directly into the

Teflon tubing because of the size of the cells. A container that was large enough to hold the cells and was capable of containing the atmospheric conditions of each line was required. The one inch diameter glass tubes with Teflon lined lids fit the requirement.

Inside of each weathering chamber is a test tube rack/support that can hold thirty-six one inch diameter test tubes in a horizontal position. This rack was made of hardwood and pressboard. Here, wood was chosen over metal because of intimate contact with the glass cell containers. It was seen as less likely to have a cell container break due to contact with wood than if it were in contact with metal.

Power transformers and heat tape were used to maintain the temperatures in high temperature chambers. The heat tape was wound around the cell containers to provide local heating to the cells. This option was a quick solution because the first choice of temperature control was not available for the weathering apparatus when it was built. The first choice was to use a heating sheet controlled by a thermostat. The thermostat and heating sheet would maintain a constant temperature inside the chambers with no intervention from the user. The current build of the weathering apparatus requires a thermometer placed inside of the chamber be checked weekly and any adjustments made manually.

For every connection between the Teflon tubing and glass components, a Teflon stopper was required (except where there was already a Teflon lid in place). Teflon was chosen to eliminate the diffusion of gases into the weathering apparatus. These Teflon stoppers were epoxied into place and sealed with a hi vacuum epoxy obtained from Master Bond, Inc. (part no. EP21TDCHT). This epoxy was used on all connections to ensure a sealed system.

There was a UV lamp installed in one of the room temperature exposure chambers. This lamp emitted in the short band UV as well as the long band UV. It was chosen over single band lamps because it was not known which band, if either, has an effect on the oxidation process. It was oriented such that the exposure to the cells would be as uniform as possible given the geometry of the chamber.

Table 21 shows the materials list for the weathering cells designed in this project. A discussion of the equipment follows. The cell designs were more limited in approach than the weathering apparatus because they had to meet several dimensional constraints which didn't affect the weathering apparatus.

Table 21: Weathering Cells Materials List

Item	Quantity	Usage	As Seen In
0.5 μ Frit	400	DRIFTS/ Luminescence /Raman Cells	Fig. 12, 13, 14
Stainless Steel Rod	100	DRIFTS Cell	Fig. 12
KRS-5 Windows (6 mm x 1 mm)	24	DRIFTS Cells	Fig. 12
Quartz Windows (6 mm x 1 mm)	12	DRIFTS Cells	
Stainless Steel Capillary Tubes	200	DRIFTS Cells	Fig. 12
Fused Silica Capillary Tubes	70	Luminescence/ Raman Cells	Fig. 13, 14
Teflon Funnel	4	Capillary Filling Jig	Fig. 15

The 0.5μ frits were chosen for air exchange purposes and to contain the sample particles. The frits were used on each type of cell with two frits on each cell which allows air to flow over the sample.

The DRIFTS cell was machined from a stainless steel rod. Stainless steel was chosen over aluminum because when roughened, stainless steel is a poorer specular reflector than roughened aluminum. Specular reflectance is not desirable in the DRIFTS measurements. KRS-5 windows were chosen as the infrared windows for the DRIFTS cell. It was chosen over ZnSe, ZnS, KBr, and diamond for multiple reasons. It was chosen over ZnSe and ZnS for bandwidth considerations. Most of the infrared structure expected is in the 400 to 1000 cm^{-1} region of the spectrum. ZnS is primarily a mid-wave infrared window and does not pass radiation in the region we are interested in. ZnSe passes radiation in a portion of the region of interest, however, it does not cover the region below 700 cm^{-1}. KBr covers the entire region of interest, but it is very hygroscopic. It reacts with the air and is very unstable. Diamond is the ideal window, as it covers the entire region of interest and it does not react with the air. The only downside to diamond is the cost. KRS-5 was chosen because it covers the region of interest, is relatively cheap (compared to diamond), and is less hygroscopic than KBr. Quartz windows were chosen as UV transmitting windows for the DRIFTS cells that were to be placed in the UV exposure chamber. Quartz transmits in the region of UV utilized and is very inexpensive (compared to the infrared windows).

Fused silica capillary tubes were chosen over borosilicate glass for the luminescence and the Raman cells. The fused silica capillaries were more expensive, but were a fluorescence free grade from ISA/Spex. The borosilicate glass capillaries were not of a consistent mixture and showed inconsistent luminescence signatures. The only advantage that the borosilicate glass capillaries had over the fused silica capillaries was in the Raman analysis. Fused silica has a Raman peak at 455 cm^{-1}, and the borosilicate glass showed no Raman peaks. Since sample was limited, it was decided that the Raman peak in the fused silica was acceptable and both cells were designed from the same materials. Therefore, the cell could be used for both luminescence and Raman scattering, thereby conserving sample. If more sample becomes available, then borosilicate glass capillaries would be the better choice for the Raman scattering analysis.

A Teflon funnel was fashioned to ease the loading of the Raman and luminescence cells. It was machined from a Teflon rod by the AFIT shop

Table 22: Dispersible Chemicals List

Chemical	Amount	Usage
UO_2	1.7 g	Standard/Weathering
U_3O_8	25 g	Standard
UO_3	50 g	Standard
CeO_2	25 g	Standard/Weathering
Diamond Dust	10 g	Standard/Weathering Dilutant
$EuCl_3$	5 g	Standard (Lum.)

Table 22 shows the amounts of dispersible chemicals available for use in this project. Note the limited amount of UO_2 available.

Appendix B: Images of Particles

In this appendix, scanning electron microscope (SEM) images of particles representative of the samples utilized in this study are presented. Cerium dioxide, diamond dust, and copper oxide are each presented. The reason that uranium oxides are not presented are due to the radiological hazards of working with dispersible sources and the necessity of the sample being imaged to be open in the chamber of the SEM system utilized. Were we to put the uranium powders into the SEM in a manner that would allow for images to be obtained, the system would likely have been contaminated with loose radioactive particles.

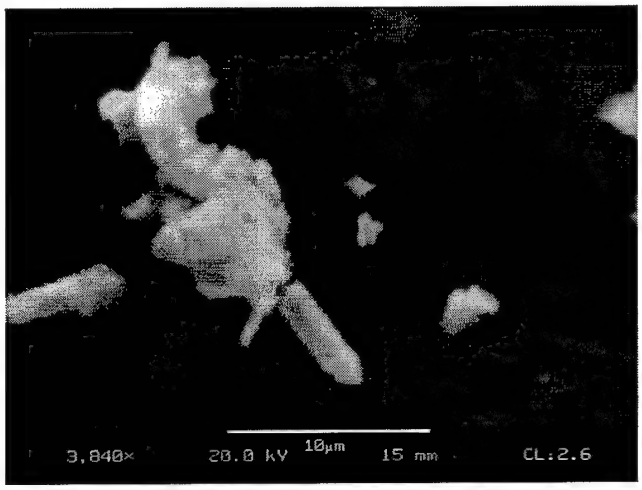

Figure 35: SEM Image of Cerium Dioxide

Also, the SEM system is located in a portion of the AFIT building that is not authorized for radioactive materials usage. It is stated that the particle sizes of the uranium oxides used here are similar to the sizes of cerium dioxide particles. Figure 35 shows an SEM image of cerium dioxide. The particles in the image are ranging in size from 1 to 8 microns. Examination of the SEM images obtained showed a particle size distribution of 1 micron to 20 microns in size.

Figure 36 shows an SEM image of a sample of diamond dust particles from the same source as those used to dilute the uranium oxides. The size of the particles are fairly uniform at 5 to 7 microns in size.

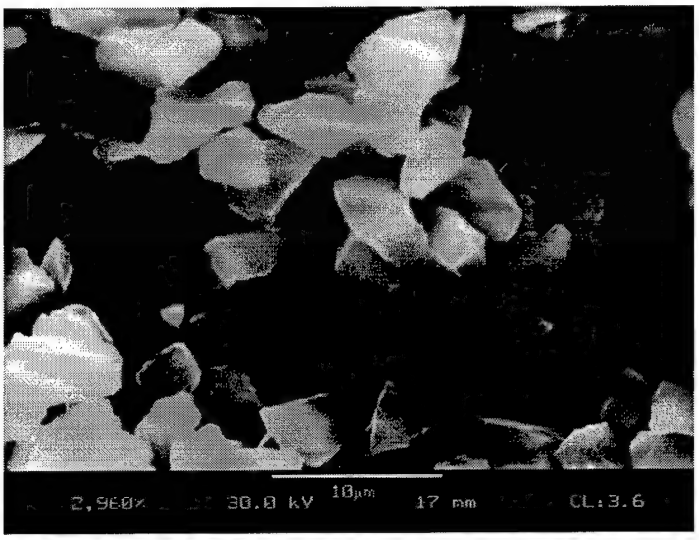

Figure 36: SEM Image of Diamond Dust

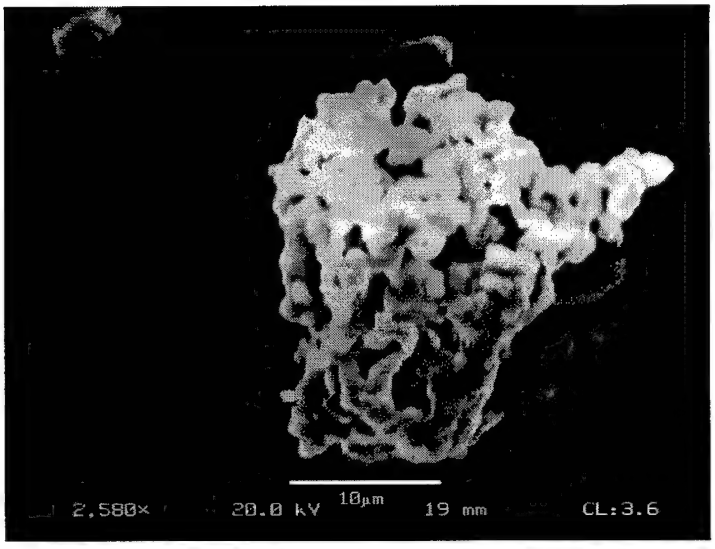

Figure 37: SEM Image of CuO Particle

The image shown in figure 37 is of the copper oxide used for the black oxide test in the NIR-Raman system. This image shows the size of this particle to be roughly 20 to 25 microns. This image was taken before any laser exposure occurred to the CuO particles.

Appendix C: Cell Loading Procedures

As mentioned in Appendix A, there are two types of weathering cells used in this analysis, the capillary cell and the stainless steel DRIFTS cell. Loading of these cells with the material is not a simple task. It is a task that requires patience and a steady hand. Procedures have been laid out which simplify the task as much as possible. These procedures are what is presented in this appendix.

There are several preparations that are common to both types of cells. Those that are cell unique are labeled with a {ss} for the DRIFTS cell or a {cs} for the capillary cell. Table 23 is a list of materials required to fill the cells. Table 24 outlines the steps necessary to fill these cells. Caution must be used whenever taking any item into or out of the glove box. When placing any object inside the glove box, ensure that the air lock outer door is closed and secured prior to opening the inner doors. This is to prevent any loose contamination that may be present inside of the glove box from escaping. Also, the integrity of the atmosphere inside the glove box will be lessened every time the air lock is opened. To maintain the integrity of the atmosphere inside the glove box, ever time the air lock is opened, the box must be flushed with nitrogen a minimum of 3 times with 5 times being recommended. When flushing the glove box, use the vacuum pump to take the box to 1.5 psi. below ambient Do not exceed a pressure difference of 2.5 psi as the glove box may buckle. Ensure that the gaskets between the top and bottom half of the glove box maintains a good seal with silicon vacuum grease lining the joint.

Table 23: Materials List for Cell Loading

Glove Box	Vacuum Pump	Nitrogen Gas Supply
Ring Stand	Spatula	Filter Paper
Capillary Block	Tweezers	28 gauge wire {cs}
KRS-5 Windows {ss}	20 gauge wire	Cells
Master Bond Epoxy Part A	Master Bond Epoxy Part B	Waste Bag (inside glove box)
Teflon Funnels {cs}		

Table 24: Cell Loading Procedures

Step Number	Procedure
1	Place all materials inside of air lock and transfer to inside of glove box. Ensure all sealing hooks are latched. Close all inlet pipes to glove box.
2	Attach nitrogen supply line to inlet port on glove box. Attach vacuum draw line to vacuum port.
3	Evacuate and refill chamber with nitrogen 5 times. Evacuate to -1.5 psi (do not exceed -2.5 psi)
4	With hands in gloves of glove box, align ring stand with capillary block at comfortable working level
5	Line floor of glove box with filter paper
6	Place cell on capillary block {ss} ensure frits and quartz window attached {cs} place in hole of capillary block
6a {cs}	Place Teflon funnel over capillary
7	Remove cap of sample container and place cap on filter paper to right of ring stand
8	Remove sample from container with spatula and place in cell. Fill to desired level. Place cap on container when finished
9 {cs} only	Use 28 gauge wire to stir sample in funnel to fill capillary to desired level, roughly one third full
9 {ss} only	Fill cell to just below frits
10 {cs} only	Seal cell with epoxy using 20 gauge wire as applicator
10 {ss} only	Apply epoxy to lip of cell using 20 gauge wire as applicator
10a {ss} only	Affix KRS-5 windows to cell
11	Place loaded cell on filter paper to right of ring stand until epoxy has set, roughly 3 hours
12	Perform radiation swipes and count to ensure no loose contamination
13	Remove completed cells through airlock and discard wire and all filter papers into "hot waste" inside of glove box

Vita

Matthew Sean Zickafoose was born on 13 September 1969 in Lima, Ohio to M. G. and Linda Zickafoose. He graduated from Bath Senior High School in Lima in 1988 and attended the University of Cincinnati, Cincinnati, Ohio, from which he received the degree of Bachelor of Science in Physics in June 1992. Upon graduation, he received his commission from the Reserve Officer Training Corps. He served as Lead Engineer, AGM-130 Air Vehicle for ASC/YG at Eglin Air Force Base, Florida until entering the School of Engineering, Air Force Institute of Technology in May 1996. He is a member of Sigma Pi Sigma.

Permanent address: Fort Walton Beach, Fl 32548

REPORT DOCUMENTATION PAGE

Form Approved
OMB No. 0704-0188

1. AGENCY USE ONLY *(Leave blank)*	2. REPORT DATE	3. REPORT TYPE AND DATES COVERED
	Dec 97	Final

4. TITLE AND SUBTITLE
Analysis of Uranium Oxide Weathering by Molecular Spectroscopy

5. FUNDING NUMBERS

6. AUTHOR(S)
Captain Matthew S. Zickafoose, USAF

7. PERFORMING ORGANIZATION NAME(S) AND ADDRESS(ES)
AFIT/ENP
WPAFB, OH 45433

8. PERFORMING ORGANIZATION REPORT NUMBER
AFIT/GAP/ENP/97D-10

9. SPONSORING/MONITORING AGENCY NAME(S) AND ADDRESS(ES)
Captain Charlie Brennan
HQ AFTAC/TMNE
1030 S. Highway A-1A
Patrick AFB, FL 32925-3002

10. SPONSORING/MONITORING AGENCY REPORT NUMBER

11. SUPPLEMENTARY NOTES

12a. DISTRIBUTION AVAILABILITY STATEMENT
Approved for public release; distribution unlimited

12b. DISTRIBUTION CODE

13. ABSTRACT *(Maximum 200 words)*

A preliminary study of the weathering of uranium oxide particles diluted in diamond dust at ambient environmental conditions is presented. The primary weathering reaction is oxidation of the uranium from the +4 to +6 oxidation state, although formation of compounds such as carbonates and hydroxides is possible. Identification of the state of uranium oxides has been attempted using luminescence spectroscopy and diffuse reflectance Fourier transform infrared spectroscopy (DRIFTS). Luminescence spectra of nominal samples of three common oxides, UO3, U3O8, and UO2, have been measured showing significant spectral differences in peaks at 494 nm, 507 nm, 529 nm, and 553 nm. DRIFTS spectra of the same three oxides show significant differences in peaks at 960 cm-1, 856 cm-1, and 754 cm-1. The differences in these peaks allow determination of the oxidation to the +6 state in these compounds.

14. SUBJECT TERMS
Uranium Oxide, Uranium, Weathering, Luminescence, Raman, DRIFTS

15. NUMBER OF PAGES
83

16. PRICE CODE

17. SECURITY CLASSIFICATION OF REPORT	18. SECURITY CLASSIFICATION OF THIS PAGE	19. SECURITY CLASSIFICATION OF ABSTRACT	20. LIMITATION OF ABSTRACT
Unclassified	Unclassified	Unclassified	UL